Sericite from the Silverton caldera, Colorado: Correlation among structure, composition, origin, and particle thickness

Dennis D. Eberl

U.S. Geological Survey, Federal Center, Mail Stop 404, Denver, Colorado 80225, U.S.A.

Jan Środoń

Institute of Geological Sciences, Polish Academy of Sciences, 31-002 Kraków, Senacka 3, Poland

Mingchou Lee

Department of Earth Sciences, Case Western Reserve University, Cleveland, Ohio 44106, U.S.A.

P. H. Nadeau*

The Macaulay Institute for Soil Research, Craigiebuckler, Aberdeen AB9 2QJ, United Kingdom

H. Roy Northrop

U.S. Geological Survey, Federal Center, Mail Stop 963, Denver, Colorado 80225, U.S.A.

Abstract

"Sericite" is a petrographic term used to indicate highly birefringent, fine-grained, micaceous material that is viewed under the optical microscope. Other analytical techniques, including X-ray diffraction (XRD) analysis, transmission-electron microscopy (TEM), and chemical analysis, reveal that sericite from the Silverton caldera is very fine grained muscovite or phengite, with a layer charge close to 1.0 equivalent per $O_{10}(OH)_2$ for the micaceous layers. The structure and chemistry of this sericite differ from that of coarser-grained micas, however, because the sericite particles are so thin that exposed basal surfaces comprise a significant proportion of the sample. The presence of these surfaces leads to swelling (expandability), to larger cation exchange capacities, and to smaller fixed cation contents in the structural formulae. These surface properties correlate with the thickness of the clay particles parallel to c^*, in agreement with the theory of interparticle diffraction. Expandability also correlates with the Kubler index (thereby suggesting that this "crystallinity" index is a function of particle thickness), with an intensity ratio (Ir), and with the wave number of an 824–834 cm^{-1} infrared absorption band. The amount of octahedral Fe + Mg can be estimated from the wave number of a 528–540 cm^{-1} infrared absorption band.

Based on XRD analysis and computer modeling, the sericites are classified as $R \geq 3$, mixed-layer illite/smectites that range in expandability from >4% to <14%. The thickness of the expanding layers is related to interlayer chemistry and to relative humidity. Expandabilities measured by a conventional XRD peak-position method are systematically smaller than expandabilities obtained by particle-thickness measurements. Better agreement is obtained when XRD peak positions are corrected by deconvolution for a contribution from unarticulated illite particles. A new method for measuring expandability uses XRD peak-breadth measurements from very thin XRD sample preparations and the Scherrer equation.

Sericite from the Silverton caldera occurs in fractures that cut a Tertiary volcanic complex and appears to have been formed by the hydrothermal alteration of fault gouge. K-Ar isotopic ages and oxygen-isotope geothermometry indicate that sericite formed during two hydrothermal events that involved heated meteoric water. It formed at about 180°C during a 21-Ma event and at about 320°C during a 13-Ma event. Sericite crystal chemistry roughly reflects temperature of formation: the younger, higher-temperature sericites have thicker micaceous particles, which means that they are less expandable, contain more fixed cations per formula unit, and have smaller cation-exchange capacities, and they have larger $2M_1$/$1M$ polytype ratios.

* Current address: STATOIL, Post Boks N4001, Stavanger, Norway.

INTRODUCTION

"Sericite" is a petrographic term used to indicate highly birefringent, fine-grained, micaceous material that is viewed under the optical microscope. Sericite is one of the most common alteration products found in rocks surrounding hydrothermal ore deposits; it is, for example, characteristic of the phyllic zone of alteration (quartz-sericite-pyrite assemblage) described by Lowell and Guilbert (1970) for porphyry copper deposits. Because of the fine grain size of sericite, little can be learned from examination with the petrographic microscope other than its mode of occurrence. However, other techniques such as X-ray diffraction (XRD) and microprobe analysis have indicated that sericites have diverse structures and chemistries (Bonorino, 1959; Shirozu and Higashi, 1972; Le Bel, 1979; Hendry, 1981; Nicot, 1981; Meunier and Velde, 1982; Omelyanenko et al., 1982; Cathelineau, 1983; Beaufort and Meunier, 1983; Horton, 1983, 1985; Parry et al., 1984). Generally, these studies have described sericites as being composed of muscovite, phengite, illite, hydromica, or mixed-layer illite/smectite (I/S), with fixed interlayer cation contents that usually are less than the structural limit of 1.0 equivalent per $O_{10}(OH)_2$.

This paper is an attempt to describe and to understand in detail the mineralogy and the origin of a suite of almost pure sericites that were collected from fractures in hydrothermally altered volcanic rocks in the vicinity of the Silverton caldera in the western San Juan Mountains of Colorado, U.S.A. It was hoped that such a characterization would aid in the development of general, crystal-chemical relations and identification techniques that can be used in future studies to unravel the geologic history of hydrothermal deposits that contain sericite.

GEOLOGIC SETTING

Samples were collected within and around the Silverton caldera, between the towns of Silverton and Ouray, Colorado. The Silverton caldera is one of several similar volcanic structures of Tertiary age in the San Juan volcanic field (Lipman et al., 1973). It is linked by the Eureka graben to the neighboring Lake City caldera (Fig. 1). Leedy (1971), who mapped rock alteration in the Silverton caldera, discovered that its northern part has mineral zonation patterns in the country rock that are similar to those described previously for porphyry copper deposits: pervasive phyllic alteration in the Red Mountain district, surrounded by propylitic alteration. The altered rocks are flows and tuffs of andesitic and rhyodacitic composition belonging to the Oligocene Silverton volcanic group. Major fracture zones usually have been altered hydrothermally. Sometimes the fracture zones contain gold-silver ore bodies or barren quartz veins; most commonly, however, they are filled with clays, such as the fractures sampled for this study. All of the fractures that were sampled lie outside the phyllic zone, as was described for the country rock, and within the zone of pervasive propylitic alteration. Most of the samples were collected from road

cuts; some were collected from abandoned mines. Most of the fractures were a few centimeters wide, but samples RM35A, RM35C, and RM35D came from an altered zone several meters wide. All samples came from within the Silverton caldera, or from the system of fractures that borders it, except for samples AR1 and AR1R, which were collected from the Eureka graben. Samples labeled LF came from an alteration zone associated with a silver deposit at the Longfellow mine, which is located at Red Mountain Pass. Clays from the fractures appear (on site) to have been formed by alteration of fault gouge.

METHODS AND MATERIALS

All samples were, in their natural state, wet, plastic clays that sometimes contained hard-rock fragments. They were stored wet in plastic bags. In the laboratory, they were disaggregated by shaking in distilled water for about 1 h. The samples were wet-sieved to separate out the >420-μm and 420–40-μm size fractions. The 40–10-μm, 10–2-μm, and <2-μm fractions were collected by sedimentation (Jackson, 1975).

Most of the samples were colored beige or brown in their natural state. White, or almost white material was produced from the <2-μm fraction by applying routine Na-acetate buffer plus Na-dithionite treatment, followed by 1N NaCl exchange (Jackson, 1975). Excess electrolyte was removed by dialysis. Samples then were checked for impurities by XRD, and monomineralic samples were analyzed for major elements by X-ray fluorescence spectroscopy (XRF; Taggart et al., 1981; A. J. Bartel, K. Stewart, and J. Taggart, analysts), and for F by selective-ion electrode. The <2-μm fractions also were saturated with Sr by washing them twice with 0.1N $SrCl_2$; the first washing took place overnight. These samples were cleaned of electrolyte by four washings in distilled water, and then were analyzed for K, Na, and Sr by atomic absorption spectroscopy (AAS; Van Loon and Parissis, 1969; D. D. Eberl, analyst).

Precision of the XRF analyses was checked against the National Bureau of Standards standard clays 97 and 98, and was found to be satisfactory for all elements except Na (<5% difference for Al, Fe, K, Si, Ti; <10% difference for Mg). XRF analyses of duplicate samples differed by no more than 2–3%. The K_2O analyses by XRF were checked by AAS. Structural formulae were calculated from the analyses using a model for the unit cell based on $O_{10}(OH)_2$. AAS data were used for Na_2O and SrO; XRF data were used for the other oxides. The calculation excluded TiO_2 from the structural formulae, because XRD indicated the presence of discrete anatase. CaO also was neglected, because it was present in such small quantities. All the formulae gave satisfactory octahedral occupancies (1.97–2.00), except for sample RM3 (1.89), which was determined by XRD to contain discrete quartz, and sample AR1R (1.94), which was determined by XRD to contain discrete chlorite.

XRD analysis was performed with a Siemens[1] D-500 automated diffraction system using a Cu tube, a graphite monochromator, and, unless noted otherwise, 1° divergence and receiving slits, 0.02° 2θ steps, and counting times of 1 s per step for oriented preparations, and 20 s per step for random preparations. XRD peak positions were corrected by external calibration against National Bureau of Standards standard reference materials 675

---

[1] The use of brand names is for identification purposes only and does not constitute endorsement by the U.S. Geological Survey.
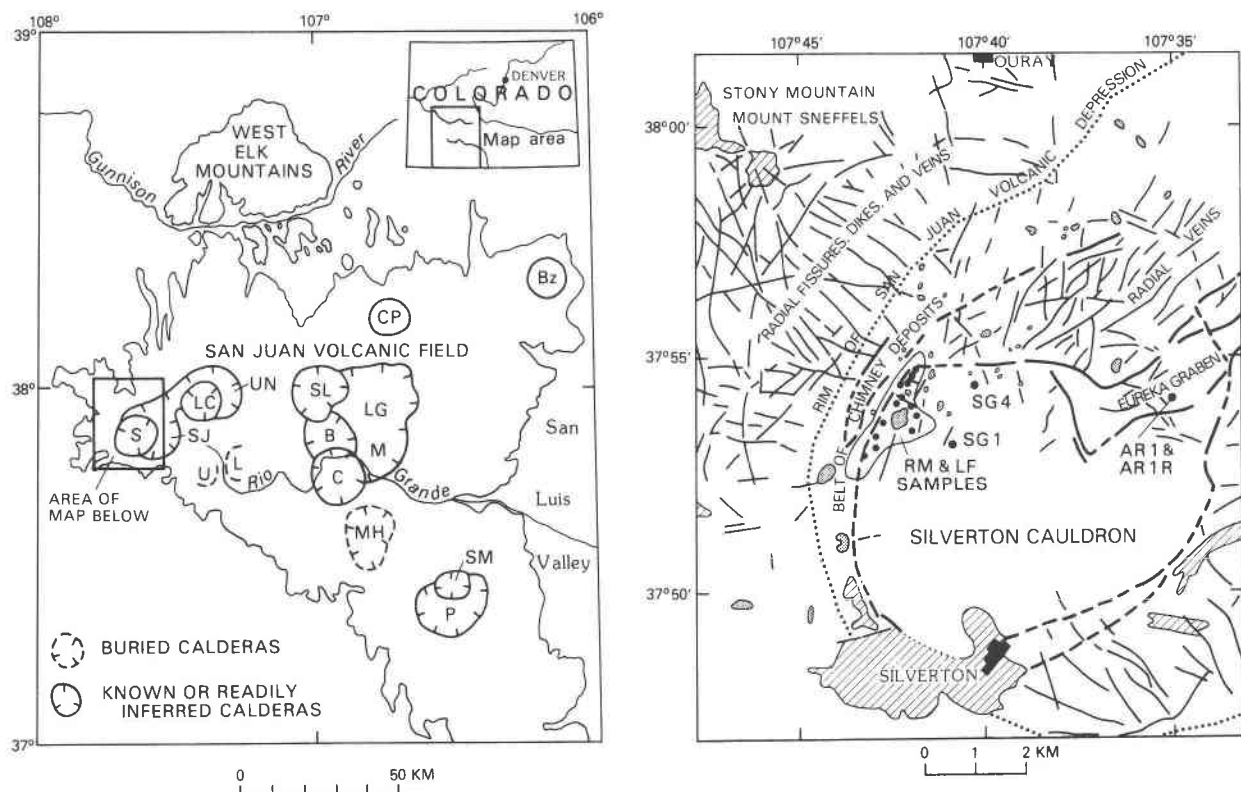
Fig. 1. Sample locations (map after Burbank and Luedke, 1961, and Lipman et al., 1970). The Silverton caldera is labeled "S," the Lake City caldera is labeled "LC," and the stippled areas are intrusive rocks.

(mica powder) and 640a (silicon powder). XRD peaks were deconvolved by using the Siemens-Allis Diffrac V/R S X peak-deconvolution program named FIT (Muller-Koelbl, 1986; based on an algorithm developed by Marquardt, 1963), and by assuming a theoretical Cauchy curve, which better matched real profiles than did a Gaussian distribution.

Oriented preparations were made by pipetting clay suspensions onto glass slides (10 mg/cm²) and were glycolated by storing in glycol vapor overnight at 60°C. X-ray slides thus prepared were equilibrated for 1 h prior to analysis in a laboratory atmosphere that had a relative humidity of 10% or less. Six subsequent measurements under these conditions indicated that reproducibility of peak positions was about ±0.01° 2θ.

Sample RM22 was investigated by XRD in Ca, K, Mg, and Sr forms; saturation was accomplished by exchange with 1N chloride solutions. The natural bulk sample and the <0.2-μm size fraction of this clay also were studied by XRD.

Infrared spectra of monomineralic, <2-μm fractions were recorded using KBr disks (proportions of sample to KBr were 1 to 100 and 1 to 1200), and a Perkin-Elmer 580B infrared spectrophotometer. Scanning-electron micrographs of bulk samples and various size fractions were made with a Cambridge Stereoscan 250 MK2 scanning-electron microscope (SEM).

Oxygen isotopes of clay and associated authigenic quartz crystals were analyzed using the technique of Clayton and Mayeda (1963). Data are presented using the standard delta notation relative to standard mean ocean water (SMOW). Fractionation factors used are from Taylor (1976), Eslinger and Savin (1973a, 1973b), and Clayton et al. (1972).

K-Ar age determinations were made on eight samples. The

K₂O analyses were made with a flame photometer on acid solutions of beads fused in lithium metaborate. Typically, 100 mg of the clay samples were analyzed for Ar; none were prebaked. Ar was analyzed with a MS10 mass spectrometer equipped with an on-line, multiloaded extraction system, and a bulb-pipetted ³⁸Ar tracer calibrated by the LP-6 interlaboratory standard at 19.3×10^{-10} mol of radiogenic Ar (^{40}Ar*) per gram. A typical clay analysis resulted in about 55–75% of the extracted Ar being radiogenic, which enables a precise measurement of the ^{40}Ar*. K decay constants used in this study are those proposed by Steiger and Jager (1977); the uncertainty in each age analysis is estimated to be 4%. However, the relative uncertainty between samples is only about 2%, because of the similar sample-preparation processes and standard solutions used for all samples.

Thicknesses of illite particles were measured by two techniques: (1) a Pt-shadowing technique using transmission-electron microscopy (TEM), as described previously (Nadeau et al., 1984a), and (2) an XRD method using very thin sample preparations and the Scherrer equation, as will be discussed below. Thicknesses determined by TEM are considered accurate to within ±4 Å for particles less than 100 Å thick; the accuracy decreases at lower magnifications employed for thicker particles.

Of the 40 samples studied, one was determined to be pure dickite, and a few collected in the vicinity of the Longfellow mine contained sodium rectorite, as was reported previously by Luedke and Hosterman (1971). The remaining samples were dominated by I/S. Some were pure I/S, except for a trace of anatase. More commonly, a small quantity of a 7-Å clay (dickite?) was present. Some samples contained quartz in the >10-μm fractions, and others contained traces of chlorite. Observations

TABLE 1. Miscellaneous properties of the samples

Sample	Color (<2 μm)	Accessory minerals*	Polytypes*
AR1	beige	goethite	$2M_1 > 1M + R$
AR1R	beige	chlorite	$1M > 2M_1$
LF7	?	jarosite (trace)	$1M + R$
LF10	beige	none	N.A.
RM3	beige	jarosite	$1M + 2M_1 + R$
RM4	beige	none	$1M \gg 2M_1 + R$
RM5	beige	none	N.A.
RM6	dark brown	jarosite (trace)	N.A.
RM8	white	jarosite (trace)	$1M > 2M_1 + R$
RM11	white	jarosite	N.A.
RM12	yellow	jarosite	N.A.
RM13	beige	pyrite	$1M > 2M_1 + R$
RM21	beige	dickite	N.A.
RM22	beige	jarosite + dicite	$1M > 2M_1 + R$
RM25	white	contains only dickite	—
RM28	beige	none	$1M \gg 2M_1 + R$
RM30	white	none	$1M$
RM31	white	pyrite	N.A.
RM33	dark brown	dickite + ?	$1M + R$
RM35A	beige	quartz + jarosite	$1M + R$
RM35C	beige	jarosite	$1M + R$
RM35D	beige	jarosite	$1M + R$
SG1	white	none	$2M_1 > 1M$
SG4	white	quartz	$2M_1$

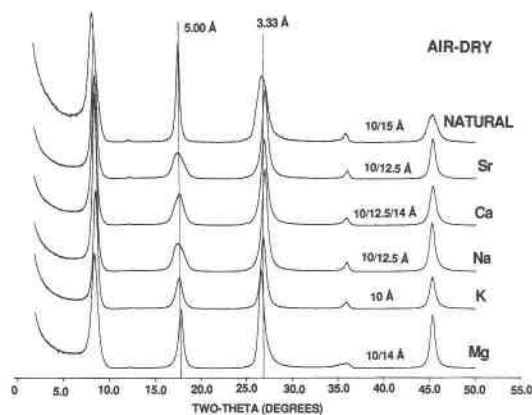* Determined by XRD of bulk samples; R = random rotations of 60 and 120°; N.A. = not analyzed.

Fig. 2. Effect of saturating cation on XRD patterns for air-dry sample RM22, with relative humidity <10%. The 10/15 Å, etc. refer to the approximate spacings of illite and expanding layers.

with the SEM indicated idiomorphic quartz crystals intergrown with sericite crystals. White samples contained pyrite, whereas beige and brown samples contained jarosite, and sometimes goethite, lepidocrocite, or gypsum. The purest I/S (Table 1) were selected for further analysis. A <2-μm-grain-size separation removed quartz and dickite, and a sodium acetate buffer plus dithionite treatment removed sulfate and iron hydroxides.

SERICITE STRUCTURE

Structure of the expanding interlayers under various conditions

XRD patterns of natural, air-dry, bulk, oriented preparations had a series of basal reflections of varying width, an indication that the sericites are mixed-layered (e.g., Fig. 2, Natural). Peak positions and intensities changed substantially after ethylene glycol solvation, indicating the presence of expandable layers (e.g., Fig. 3, Natural). Natural samples were identified as $R \geq 3$ ordered, mixed-layer I/S using the criteria of Środoń (1984).

Further experimentation indicated that the number of interlayer water or glycol layers is a function of saturating cation and relative humidity. Natural samples were determined to contain one or two water-layer complexes, with two water-layer complexes being dominant, by using criteria obtained by computer simulation (Horton, 1983). The shapes and positions of the reflections at about 5 Å and 3.33 Å are characteristic for these complexes. If the 12.5-Å (one water-layer) complex is present, the 5-Å reflection is broad, weak, and displaced toward smaller angles of 2θ from the illite peak position. The 3.33-Å reflection is sharp, strong, and displaced slightly toward larger angles. For the 15-Å (two water-layer) complex, the 5-Å reflection is strong, sharp, and not displaced, whereas

the 3.33-Å reflection is diffuse and is displaced toward smaller angles (e.g., Fig. 2, Natural).

The change in interlayer solvation related to saturating a sample with various exchange cations was investigated using sample RM22, one of the more expandable samples. The data are presented in Figures 2, 3, and 4 and were obtained at a laboratory relative humidity of 3–10%. Air-dry, Na- and Sr-saturated samples contain one water-layer (12.5-Å) complexes, according to Horton's criteria (Fig. 2). The K-saturated sample has peak positions so close to illite that it can be assumed that most of the expandable layers have collapsed to approximately 10 Å. This collapse is reversible, however, because Sr saturation of the K sample restores expandability. A Mg-saturated sample fits neither the 12.5-Å model, nor the 15-Å model: both the 5-Å and the 3.33-Å peaks are sharp. The former is displaced toward larger, and the latter toward smaller, angles of 2θ relative to illite peak positions. These peak positions indicate that the water-layer complex is about 14 Å thick. A Ca-saturated sample contains both 12.5-Å and 14-Å complexes.
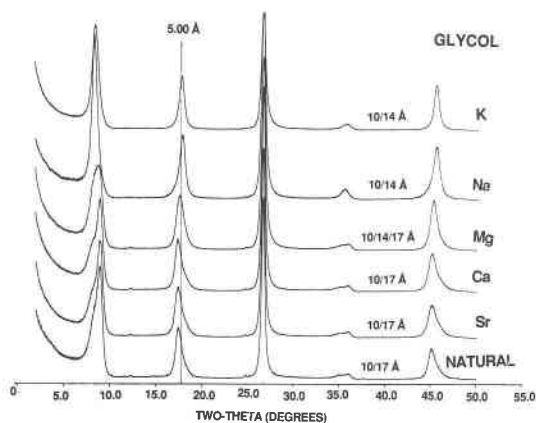

Fig. 3. Effect of saturating cation on XRD patterns for glycolated sample RM22, with relative humidity <10%.
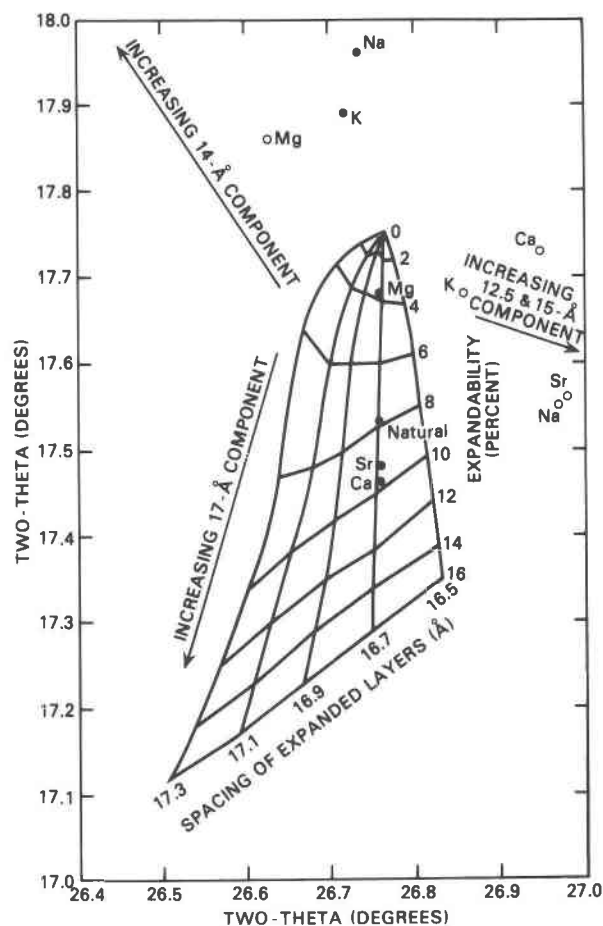
Fig. 4. A net constructed from the calculations in Table 2, on which have been plotted 2θ XRD peak positions found for sample RM22 saturated with various cations. Open circles are for air-dried samples. Solid circles are for glycolated samples.

When glycolated (Fig. 3), the K- and Na-saturated samples have similar XRD patterns. All their peaks shift in the opposite direction from that expected for I/S; instead they fit a model for illite/vermiculite (I/V) interstratification (Fig. 4). However, the vermiculite layers must be thinner than 14 Å, because the 2-Å reflection near 45° 2θ shifts toward larger angles after glycolation, and the 3.33-Å reflection is displaced only slightly toward smaller angles. XRD patterns of glycolated Sr and Ca samples (dithionite-treated, <2-μm fractions) resemble those of the natural, bulk samples (Fig. 3); they are identified as $R \geq 3$, mixed-layer I/S (Środoń, 1984). The glycolated Mg samples have patterns that are intermediate between those of I/S and I/V, thereby suggesting a three-component 10/14/17-Å system.

The previously discussed information is summarized in Figure 4 by plotting the precise 2θ positions of the 5-Å and 3.33-Å peaks of sample RM22 onto a theoretical diagram used to determine illite contents and glycol spacings for R1 and R3 I/S. Arrows in Figure 4 show the directions that the peaks will shift from the illite position,

given various thicknesses for the expandable layers. Several other sericite samples were studied similarly, and they confirmed the findings for RM22.

The discovery of vermiculite-like spacings for expandable layers in the Na sample was a surprise, because previous studies of Na clays having similar expandabilities have determined that they behave like I/S (e.g., Środoń, 1984, Figs. 1 and 2). A few samples from the cited study were re-run and found to be I/V. It is tentatively concluded that differences in relative humidity between Denver, Colorado, U.S.A. (<10%), and Kraków, Poland (>40%), are responsible for these differences in spacings for the expanded layers. It was known that relative humidity affects the thickness of smectite-type interlayers having two glycol-layer complexes (Środoń, 1980), but this is the first report of the transition from a two glycol-layer to a one glycol-layer vermiculite-like complex, in response to a decrease in relative humidity.

Expandability measurements by XRD (conventional method)

Precise measurements of expandability (percentage of swelling interlayers) for I/S depend on knowing accurately the thicknesses of the illite and the smectite layers. The illite-layer spacings of K-mica-like layers in mixed-layer clays have been determined to depend on chemical composition; they may vary from 10 Å for illite to 9.85 Å for leucophyllite (Sokolova et al., 1978). The spacings of smectite layers have been determined to depend on saturation cation, layer charge, and relative humidity (Środoń, 1980); they may vary several tenths of an ångström for two glycol-layers.

The spacings of illite layers were determined for eight samples by saturating the clays with K, heating them for 1 h at 250°C, and X-raying them in a cell at 0% relative humidity. Illite-layer spacings then were calculated from the average spacings determined from measurements of the positions of the 002 through 004 XRD reflections. Spacings for the eight samples varied from 9.967 to 10.000 Å, with a mean of 9.99 Å, a value that was used in all subsequent calculations. The same value was determined by plotting the positions of the 002 and 003 reflections for all glycolated Sr samples onto a figure similar to Figure 4 (see Fig. 2 in Środoń, 1984), and then by extrapolating these plots to a pure illite end member having an infinite crystallite thickness.

Glycol spacings and expandabilities were determined by plotting peak positions for Sr-saturated samples onto a graph similar to Figure 2 in Środoń (1984), but modified to reflect a spacing for illite layers of 9.99 Å, a crystallite thickness of 40 to 50 layers (close to infinitely thick with respect to the X-ray beam), maximum R3 ordering, 0.8 K per half-unit cell, and no octahedral Fe (Fig. 4). These calculations were made using the computer program NEWMOD (available from R. C. Reynolds, Department of Earth Sciences, Dartmouth College, Hanover, NH 03755, U.S.A.), which is a version of the computer program described by Reynolds (1980), but modified to

TABLE 2. Calculated xrd peak positions for I/S (CuK$_\alpha$ radiation)

Expandability (%)	Position of xrd reflections (°2θ)									
	16.5 Å		16.7 Å		16.9 Å		17.1 Å		17.3 Å	
0	17.75	26.77	17.75	26.77	17.75	26.77	17.75	26.77	17.75	26.77
2	17.72	26.78	17.72	26.77	17.73	26.76	17.73	26.75	17.74	26.74
4	17.67	26.79	17.67	26.77	17.68	26.74	17.69	26.72	17.72	26.71
6	17.61	26.80	17.60	26.76	17.60	26.73	17.60	26.70	17.64	26.67
8	17.55	26.80	17.53	26.76	17.50	26.72	17.48	26.68	17.47	26.64
10	17.49	26.81	17.45	26.76	17.42	26.71	17.38	26.65	17.34	26.60
12	17.44	26.82	17.39	26.76	17.35	26.69	17.30	26.63	17.25	26.57
14	17.39	26.83	17.34	26.75	17.29	26.68	17.23	26.61	17.18	26.54
16	17.35	26.83	17.29	26.75	17.23	26.67	17.17	26.59	17.12	26.51

include a faster algorithm so that thicker crystallites can be calculated (Bethke and Reynolds, 1986). The calculated 002 and 003 peak positions from which Figure 4 was constructed are given in Table 2. Thicknesses for the expanded layers determined from Figure 4 ranged from 16.5 Å to 17.3 Å, with a mean value of 16.8 Å.

Expandabilities measured by this method are given in Table 3 in the column labeled "conventional." Expandabilities are reported to one decimal place, rather than rounded off to whole numbers, because the one-decimal-place numbers result in better correlation coefficients during regression analysis and because they are reproducible. Also, as will be discussed below, small differences in expandability for I/S result from big differences in particle thickness as clays become increasingly illitic. For example, a change from 3.0% to 2.5% expandable is equivalent to a change in mean particle thickness of about 70 Å. Representative patterns of Sr-saturated I/S having a range of expandabilities are given in Figure 5.

Sr was chosen as the standard saturating cation for measuring expandabilities, because the structure of interlayers saturated with Sr^{2+} is less sensitive to changes in relative humidity than are those saturated with monovalent cations. Also, Sr saturation gives a better measure of cation-exchange capacity, because Sr^{2+} is less subject to replacement by hydronium ions during washing and dialysis than are monovalent cations (Schramm and Kwak, 1980) and because Sr^{2+} is less subject to the formation of interlayer, monovalent hydroxide species than are divalent cations of greater ionic potential. Ba has a lower ionic potential than Sr^{2+}, but this ion is toxic, and is difficult to analyze by aas; therefore it was avoided.

Expandability measurements by tem

Expandability also can be calculated from tem data if it is assumed that X-ray diffraction effects for I/S result from interparticle diffraction (Nadeau et al., 1984a, 1984b). This concept proposes that illite particles stack

TABLE 3. xrd data for sericites

Sample	Glycol complex (Å)	Expandability methods (%)					Ir	Kubler index (mm)	Hb$_{rel}$
		Conventional	Deconvolved	Scherrer		TEM*			
				17° peak	26° peak				
AR1	16.5 (?)	0	4.8	4.5	5.2	N.A.	1.31	3.8	232
AR1R	16.5	3.4	6.6	6.6	7.1	N.A.	1.59	6.3	384
LF7	16.9	4.8	8.1	7.5	8.1	N.A.	2.55	6.3	384
LF10	16.8	5.9	8.5	8.4	8.6	N.A.	2.37	7.4	451
RM3	16.9	3.2	6.1	6.4	6.8	5	1.60	5.5	335
RM4	16.8	4.3	8.0	8.1	7.6	N.A.	1.90	6.9	421
RM5	16.9	5.0	8.9	9.0	8.4	N.A.	2.26	8.0	488
RM6	16.8	6.6	9.7	7.8	9.4	N.A.	N.A.	7.1	433
RM8	16.9	6.9	10.7	11.4	10.1	N.A.	3.71	7.0	427
RM11	17.1	8.0	10.1	13.0	8.0	N.A.	3.58	6.7	409
RM12	17.3	7.8	7.9	12.2	10.5	N.A.	4.72	7.8	476
RM13	16.8	8.1	10.6	9.2	8.8	13	3.40	6.2	378
RM21	16.7	6.1	9.2	10.2	10.6	N.A.	2.78	9.7	591
RM22	16.8	9.0	12.0	9.9	13.1	N.A.	N.A.	8.2	500
RM28	16.7	3.3	8.2	8.2	8.1	N.A.	2.11	6.9	421
RM30	17.0	6.2	8.2	7.8	8.3	9	2.21	7.2	439
RM31	16.7	3.3	6.0	7.2	7.4	N.A.	1.95	6.1	372
RM35A	16.8	9.0	13.0	10.7	7.7	N.A.	3.33	7.6	463
RM35C	16.8	6.6	9.7	11.4	10.5	N.A.	2.84	7.4	451
RM35D	17.0	6.7	8.2	11.4	11.5	N.A.	3.22	11.6	707
SG1	16.9	2.7	4.9	4.1	5.1	N.A.	1.39	5.1	311
SG4	16.9	2.8	5.4	5.0	4.4	2	1.53	4.6	280

* N.A. = not analyzed.

A

GLYCOL

RM 12

RM13

RM21

RM29

SG4

TWO-THETA (DEGREES)

B

AIR-DRY
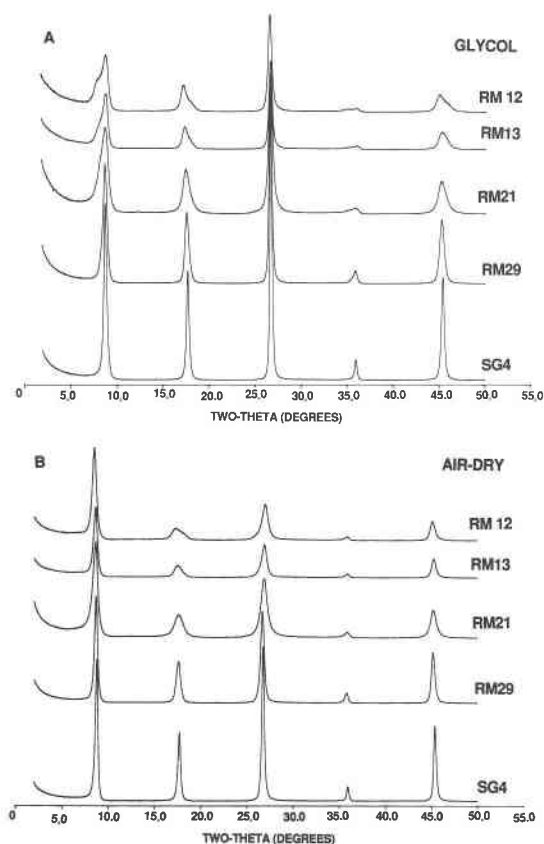
RM 12

RM13

RM21

RM29

SG4

TWO-THETA (DEGREES)

Fig. 5. Examples of XRD patterns for samples having a range of expandabilities. (A) Patterns for glycolated, Sr-saturated samples. (B) Patterns for air-dried, Na-saturated samples. Humidity <10%.

Fig. 6. TEM images of fundamental illite particles for two samples. The bars are 0.5 μm.

on top of each other on the XRD slide, absorbing water and glycol on external, planar a-b interfaces, thereby forming "smectite" layers when examined by XRD. TEM images of individual illite particles are given in Figure 6. A TEM image of illite particles showing a stacked configuration is presented in Środoń and Eberl (1984, Fig. 3); such a configuration is diagrammed in cross section on the left side of Figure 7. According to this model, expandability is related to mean illite-particle thickness parallel to c^* (Tm, in ångströms) according to

$$\text{Expandability (\%)} \approx 1000/\text{Tm}. \quad (1)$$

A more rigorous expression is Expandability (%) = 100/$(n + 1)$, where n is the number of illite interlayers in a particle, and $n = (\text{Tm} - 9.2)/9.99$, assuming that the particles end in tetrahedral sheets. The 9.2 is the thickness of a 2:1 layer (pyrophyllite spacing).

TEM expandabilities for four samples (Table 3) have been calculated from mean particle-thickness measurements (Table 4). The TEM expandabilities generally are larger than those determined by the conventional XRD method. Previously, Nadeau (1985) determined that TEM predicts 5 to 15% more smectite layers than does XRD for I/S that is less than 40% expandable. This is an important
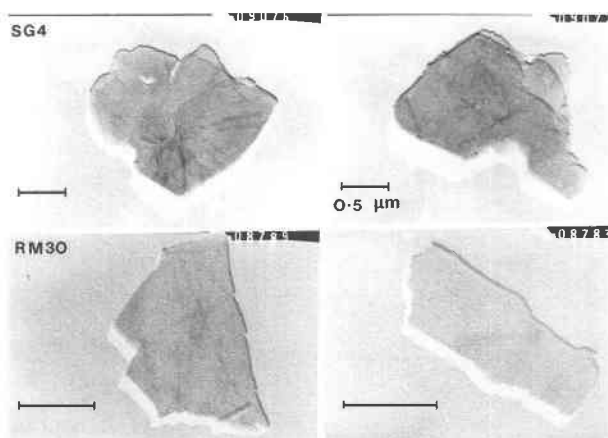
observation, because if true smectite interlayers exist within illite particles, TEM would predict *less* expandability than XRD.

Expandability measurements by XRD peak deconvolution

The discrepancy in expandabilities between XRD and TEM determinations can be explained by enlarging on the original concept of interparticle diffraction. XRD may give smaller expandability measurements, because the proportion of swelling basal surfaces between illite particles, as measured by XRD, does not necessarily correspond to the proportion of total free basal surfaces, as measured by TEM. Some illite particles may not articulate with other illite particles (right side of Fig. 7), thereby contributing to composite XRD peaks that owe their 2θ position to the combined diffraction effects of both I/S and thin, nonswelling illite (i.e., the discrete illite peak pulls the I/S peak to lower apparent expandabilities). This situation is modeled in Figure 8 for sample RM11. The resultant profile was calculated by mixing an I/S pattern (10% expandable) with an illite pattern (0% expandable) in the proportion 5:1.

If some illite particles are disarticulated and do not interact with adjacent particles, then the position of the I/S peak used above to measure expandabilities by the conventional procedure (Table 3) is incorrect, because of the effect of the discrete illite peak. To measure expandability accurately, the composite peak between 17° and 18° 2θ needs to be deconvolved into its I/S component and its illite component. This deconvolved expandability is the expandability that would be measured by XRD without deconvolution if all the diffracting illite particles were perfectly articulated. If the interparticle-diffraction concept is correct, this expandability should equal the expandability measured by TEM (and be related to particle thickness by Eq. 1) and should correlate better with surface properties, such as cation-exchange capacity (CEC) and surface area.

One problem with deconvolving peaks between 15° and

TABLE 4. TEM particle thickness measurements for sericites (parallel to c^*, in ångströms)

Sample	Tm	S.D.	L	S	n
RM3	187	234	1081	48	19
RM13	79	40	205	41	22
RM30	109	81	437	37	32
SG4	427	278	1275	93	30

Note: Tm = mean particle thickness, S.D. = standard deviation, L = largest observation, S = smallest observation, n = number of observations.

20° 2θ is that I/S has either one or two peaks in this region, depending on expandability. Two distinct I/S peaks are present when expandability equals 15%; one I/S peak with a high-angle shoulder is present when expandability equals 10%; and only one peak is present when expandability equals 5% (Fig. 4.12 in Reynolds, 1980). The strategy adopted was to deconvolve three peaks between 15° and 20° 2θ fixing the spacing for the illite peak at the previously determined 002 value of 4.995 Å (17.757° 2θ). If the position of the less-intense I/S reflection was determined by deconvolution to be on the low-angle side of the 002 illite peak, then deconvolution for these samples was repeated, using a two-peak model. The 003 peak at about 26.6° could not be deconvolved accurately, because reflections for I/S and illite are spaced too closely; therefore the nondeconvolved position of this peak in combination with the deconvolved 002 peak was used to measure expandabilities listed in Table 3.

For three out of four samples, expandabilities measured by deconvolution better match those determined by TEM than do expandabilities determined by the conventional XRD procedure. XRD patterns were calculated for one sample (RM11) for both the conventional model and the deconvolution model (2° to 50° 2θ), but the profiles looked so similar that they could not be used to distinguish which model is correct at the present level of analysis.

Expandability measurements by the Scherrer equation

It should be possible to eliminate XRD peak broadening caused by swelling by preparing an oriented XRD sample that is so thin that it is composed of a single plane of individual illite particles, rather than of the stacks of illite particles diagrammed in Figure 7. Then XRD peak breadth at half height is a function of the average thickness of illite particles parallel to c^*, once the breadth has been corrected for machine broadening. Illite-particle thicknesses (Tm) can be calculated from such measurements by using the Scherrer equation, and expandabilities can be calculated from Tm by using Equation 1.

The Scherrer equation (Klug and Alexander, 1974) is

$$Tm = K\lambda/\beta \cos \theta, \qquad (2)$$

where K is a constant that is equal to 0.91 (Brindley, 1980), λ is the wavelength of CuK_α radiation (1.541 81 Å), and β is the XRD peak width at half height in radians (1° = 0.017 45 radians). β was corrected for machine
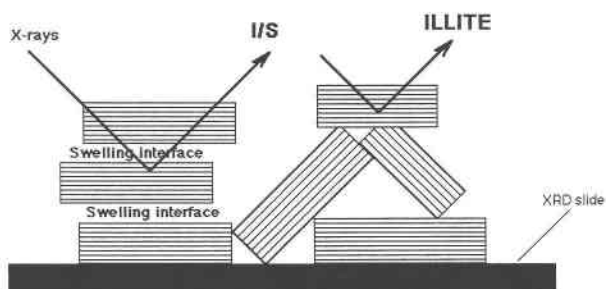

Fig. 7. Schematic diagram showing illite particles (see Fig. 6), each composed of many illite layers, aligned in oriented aggregates on an XRD slide. Interparticle diffraction causes diffraction effects for I/S in aggregates in which the particles are articulated, and diffraction effects for nonexpanding illite where particles are not articulated. The XRD pattern is the summation of diffraction from these two types of scattering domains.

broadening (Brindley, 1980) using the National Bureau of Standards mica powder as a standard. A very thin layer of oriented sample was dispersed on an Al slide in an attempt to remove peak broadening caused by mixed layering. An Al rather than a glass slide was used to avoid
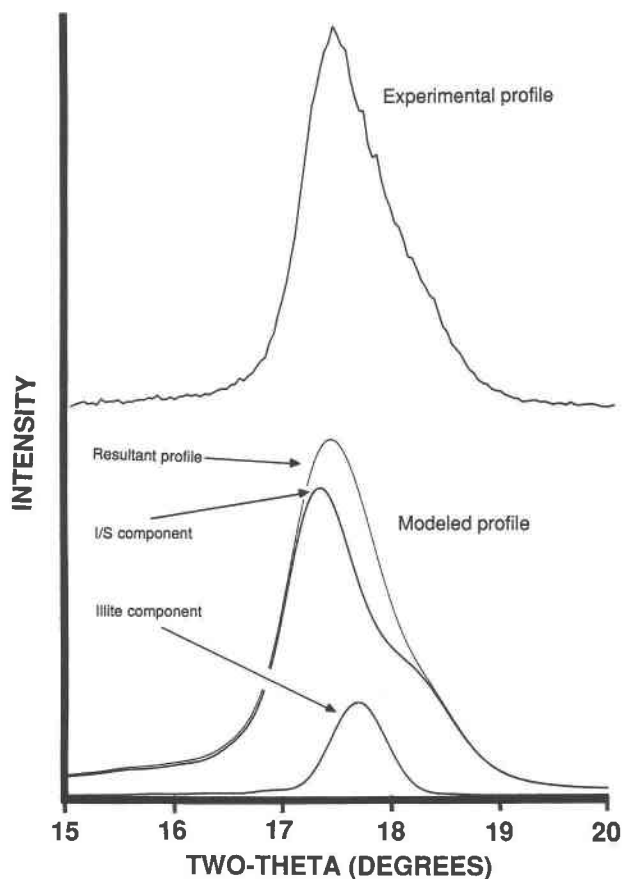

Fig. 8. Experimental XRD profile (top) for sample RM11 (glycolated and Sr saturated) and the suggested two-component model (bottom). Model was calculated using a modified version of the computer program of Reynolds (1980).

TABLE 5.　XRD results from X-raying progressively thinner preparations of glycol-solvated sample RM30A (CuK_α radiation)

| Clay concentration (mg/cm²) | XRD peak positions (°2θ) | | Expandability methods (%) | | | | |
	Conventional	Deconvolved	Conventional	Deconvolved	Scherrer 17° peak	Scherrer 26° peak	Ir
8.72	17.629	17.491	5.7	7.7	8.5	5.7	1.47
4.35	17.642	17.490	5.5	7.7	8.4	5.7	1.61
2.18	17.636	17.495	5.6	7.7	8.2	5.4	1.60
1.34	17.650	17.497	5.4	7.6	8.1	5.6	1.63
0.87	17.659	17.506	5.2	7.6	8.1	5.7	1.38
0.63	17.675	17.494	4.8	7.7	8.1	5.8	1.51
0.47	17.711	*	3.6	*	7.4	6.2	1.23
0.22	17.712	*	3.6	*	7.8	6.3	1.16
0.10	17.713	*	3.6	*	7.0	6.5	1.11
0.07	17.740	*	1.7	*	9.2	8.3	1.22
0.03	17.768	*	<0	*	5.8	7.3	0.99
0.01	17.737	*	2.3	*	5.8	6.4	0.84

* Could not be deconvolved.

interference in the XRD pattern from the amorphous glass hump.

Results found from X-raying progressively thinner preparations of sample RM30A (a recollection of sample RM30) are given in Table 5. The table shows that apparent expandabilities measured by the conventional method remain constant at about 5.6% for the first three concentrations. Then the apparent expandabilities decrease regularly with decreasing concentration until a second plateau is reached at 3.6% expandable. The last three concentrations give erratic expandabilities. Deconvolved expandabilities, however, remain constant at about 7.7% expandable throughout the concentration range, until a concentration is reached at which the peaks no longer can be deconvolved. This concentration corresponds to the 3.6% plateau in the apparent expandabilities mentioned previously. Expandabilities calculated by the Scherrer equation for clay concentrations at this plateau, using the breadth of the 17° peak, average 7.4%, an expandability that corresponds favorably to 7.7% found by deconvolution. The breadth of the 26° peak gives an average expandability of 6.3% at this plateau. Intensity ratios (Ir, to be discussed below) along this plateau are close to 1.0 (1.1 to 1.2).

These experimental results are explained as follows. The first plateau in the apparent expandabilities corresponds to a situation in which the clay preparation is thicker than the mean defect-free distance parallel to c^* in the stacks of illite particles that diffract as I/S crystallites. As the preparation becomes thinner than the defect-free distance, however, the proportion of discretely diffracting illite particles increases, thereby giving lower apparent expandabilities, until the preparation is so thin that it diffracts *as though* it is a single layer of illite particles. The 2θ angle found for this second plateau (17.71°, Table 5) is that expected for nonexpanding, very thin illite, after its peak position has been corrected for a shift from the infinitely thick illite crystal (17.757°). The shift is caused by an interaction between peak broadening, related to fine particle size, and a rise in low-angle X-ray intensity, related to the Lorentz-polarization factor. The last three apparent expandabilities are erratic, because X-ray intensities are so small for these very dilute preparations that peak positions cannot be determined accurately. The deconvolved expandabilities remain constant, because deconvolution removes peak shifts related to diffraction from discrete illite, as was discussed above. Peaks cannot be deconvolved when the second plateau in apparent expandabilities is reached, because only one peak, that for pure illite, is present. The presence of nonexpanding illite in these preparations also is indicated by an Ir that is close to 1.0 (see below). Expandabilities determined by deconvolution are approximately equivalent to those determined by the Scherrer equation, as is to be expected if the theory is correct. An exact correspondence in expandabilities measured by the two methods is not always to be expected, however, because the position of the illite peak that was assumed to be constant at 17.757° during the deconvolution routine actually will vary with illite particle thickness, as was discussed above.

Similar analyses of two other samples (samples SG4 and RM13) indicated that a concentration of 0.10 mg/cm² was good for determining expandabilities from the Scherrer equation for this suite of sericites. Al slides having this concentration of Na-saturated clay were X-rayed air-dry in the laboratory atmosphere using 3° divergence and receiving slits, and 0.02° 2θ steps, with 10 or 20 s per step. The results are reported in Table 3 for both the 17° and the 26° 2θ peaks.

Expandabilities measured by deconvolution, by the Scherrer equation, and by TEM are compared with expandabilities measured by the conventional method in Figure 9. The curves for the XRD techniques are nearly coincident, but the TEM curve differs. The TEM curve is based on only four data points, and the thickness measurements used to construct the curve have large standard
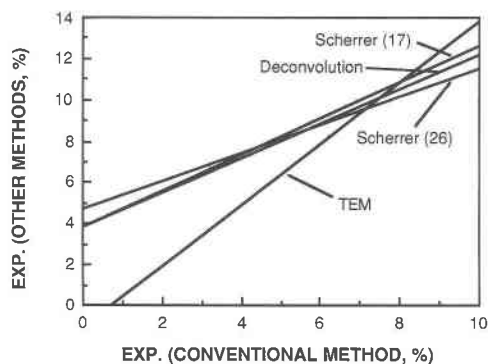
Fig. 9. Relation between expandability (exp.) measured by the conventional method and expandabilities measured by the Scherrer and peak-deconvolution methods.

Fig. 10. Relation between expandability and the intensity ratio (Ir).

deviations (Table 4). Therefore, we are reluctant to apply the TEM data quantitatively and have not emphasized them in subsequent discussions. More TEM data would be required to solve the problem of which experimental technique gives the more accurate expandabilities. Correlation coefficients (R) for the curves in Figure 9 range from 0.78 to 0.89 for the XRD techniques; R is 0.97 for the TEM curve.

The Scherrer equation is the simplest method for measuring expandabilities for sericites. Deconvolution programs and programs for calculating mixed-layer clay structures are not required. In addition, it is not necessary to know the thickness of the glycol complex, or to make assumptions during deconvolution about the 2θ angle of the discrete illite peak. The method requires neither a transmission-electron microscope, nor many measurements of a single sample to insure an accurate determination of mean particle thickness. An intensity ratio (see below) close to 1.0 and the determination of similar expandabilities from the breadths of two or more XRD peaks indicate that the sample is thin enough to avoid peak broadening related to swelling.

Relation between expandability and intensity ratio (Ir)

Although peak shifts are small and difficult to detect for samples having very small expandabilities, traces of expandability can be detected by using the intensity ratio (Ir) introduced by Środoń (1984):

$$\text{Ir} = (001)/(003)_{\text{air-dried}}/(001)/(003)_{\text{glycol}}. \quad (3)$$

Qualitatively, the intensity ratios in Table 3 favor the peak-deconvolution and the Scherrer equation methods for measuring expandabilities, because a sample that gave 0% expandable by the conventional peak-position method of measurement (sample AR1) has Ir > 1.0, thereby indicating that it is expandable, a result that agrees with the deconvolution and the Scherrer methods.

A plot relating expandabilities, measured by the Scherrer method (using the 27° peak), and intensity ratios is given in Figure 10. The equation given in the figure probably is valid for expandabilities less than about 8% and
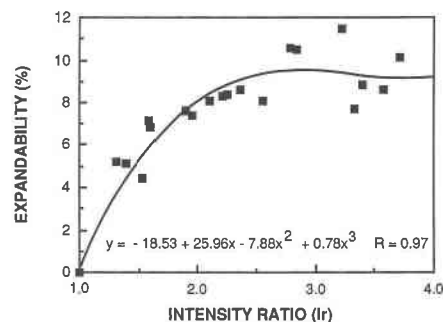
for sericites having chemistries similar to those examined in the present study. The theoretical end point, Ir = 1.0, expandability = 0%, is included in the regression analysis and has been measured for the Kaube sericite (Środoń and Eberl, 1984). Equations for the correlation between Ir and expandabilities measured by using the breadth of the 17° peak and by peak deconvolution are very similar to the equation given in Figure 10. The equation relating Ir to expandabilities measured by TEM, however, is $y = -10.2 + 11.3x - 1.5x^2$, with $R = 0.98$.

Relation between expandability and measurements by infrared (IR) spectroscopy

Infrared data from Sr-saturated samples (Table 6 and Figs. 11 and 12) indicate an approximate correlation ($R = 0.82$) between expandability, measured by the Scherrer method (26° peak), and the absorption band that migrates between 826 and 833 wave numbers. Correlation coefficients for expandabilities measured by the breadth of the 17° peak and by deconvolution are $R = 0.80$ and $R = 0.81$, respectively. The TEM data (three points) give the equation $y = 1873.5 - 2.25x$, with $R = 0.98$.

Relation between expandability and the Kubler index

The Kubler index is the width at half height in millimeters of the illite 001 XRD reflection (see Kisch, 1983, for a review). Figure 2 indicates that the type of saturating cation may influence this measurement. Kubler indices for <2 μm, Sr-saturated, air-dry sericites are listed in Table 3 and were calculated by assuming that 1° 2θ equals 10 mm on the X-ray chart (see Kisch, 1983, Table 5-IV). The correlation between Kubler indices and expandabilities measured by the Scherrer method (26° peak) for our experimental system is shown in Figure 13 ($R = 0.80$). The relation is Expandability ≈ Kubler index + 1.3. Extrapolation with this equation to 0% expandable shows that the relation must be nonlinear at very small expandabilities. Other expandability methods used for measuring expandabilities for this correlation gave $R = 0.70$ (Scherrer, 17° peak), 0.52 (deconvolution), 0.61 (conventional method), and 0.76 (TEM method). A measurement that is related to the Kubler index, Hb_{rel} (the relative peak width at half height of the 001 illite peak with respect to
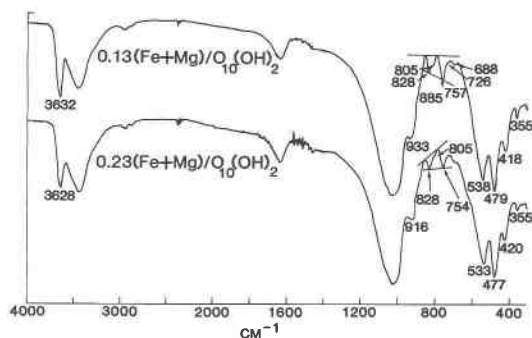
Fig. 11.   Sample infrared absorption spectra for two samples having contrasting octahedral cations (see Table 8). Sample RM12 (top) and sample RM13 (bottom).
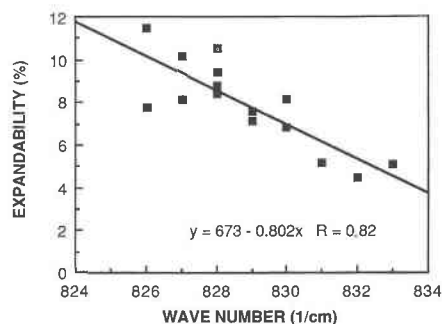

Fig. 12.   Relation between expandability (Scherrer method, 26° peak) and wave number for the infrared-absorption band that migrates between 826 and 833 cm^{-1}.

the 100 quartz reflection at 20.85°; see Kisch, 1983), also is reported in Table 3.

Polytype analysis

Preliminary study of randomly oriented, natural samples detected a range of polytypic varieties, including pure $1M$ and $2M_1$ polytypes, and mixtures of these polytypes with variable degrees of disorder. Data for different size fractions (Fig. 14) indicate that the (*hkl*) characteristics of the sericites are independent of grain size, unlike illites from shale that were determined to have an increase in the $2M_1$ component with increasing grain size (e.g., Środoń and Eberl, 1984). In the sericites, $2M_1$ and $1M$ clays are not physically separable by size, which implies that either the two polytypes have the same grain size or they exist as separate X-ray scattering domains within the same crystallites.

The only systematic variations detected with changing grain size are a sharper rise in background at smaller angles and a more intense band between 22° and 33° 2θ for the finer fractions (Fig. 14A). Computer simulation

(Drits et al., 1984) has indicated that this band results exclusively from rotational stacking faults ($\pm60°$ or $\pm120°$). Thus, the density of rotational faults increases in the finer fractions of the sericites. In sample RM30, which is a pure $1M$ polytype, the appearance of rotational stacking faults is negligible (Fig. 14B).

For most samples polytypes were studied in the <2-μm fractions. The range of variation encountered is shown in Figure 15 and is listed in Table 1. Clays that are <6% expandable (Scherrer method) are dominantly $2M_1$ (e.g., sample SG4 in Fig. 15). XRD reflections for $2M_1 + 1M$ mixtures are strong and sharp, indicating that the $2M_1$ and $1M$ domains must be relatively thick, although the height of the 22°–33° 2θ band sometimes indicates abundant rotational faults. Clays that are >6% expandable are dominated by $1M$ structures. In two samples, perfect $1M$ structures were detected, as evidenced by the sharpness of the peaks and by the absence of the 22°–33° 2θ band (e.g., Fig. 14, sample RM30). Sample RM30 represents the T variety of illite (*trans* sites vacant in the octahedral sheet), as calculated by Drits et al. (1984), as is indicated

TABLE 6.   Infrared (IR) absorption data for sericites

Sample	Infrared absorption bands (cm^{-1})														
AR1	3628	1075d	1023	—	913	831	805	754	—	685	564	530	475	420	356
AR1R	3627	1069	1026	—	914	829	Q	753	725tr	d	tr	531	478	425	356
RM28	3625d	1067	1026	—	914	830	805sh	754	—	d	565	535	478	420	353
RM13	3628	1066	1026	—	916	828	805sh	754	—	d	tr	533	477	420	355
RM4	3628	1065	1029	—	916	829	Q	755	—	d	565	532	478	420	356
RM5	3625	1067	1023	—	917	828	803	755	—tr	d	tr	534	477	420	353
RM6	3628	1067	1028	935<	915	828	805	755	725tr	d	tr	537	478	419	353
RM3	3628	1068	1035	935<	915	830	Q	754	—tr	d	tr	535	478	420	353
RM29	3632	1067	?	935<	913	829	805	756	727	d	565	537	480	416	357
RM35A	3623d	1066	1031	935=	915	826	sh	755	725tr	d	tr	539	482	420	tr
RM8	3623d	1065	1026	935=	915	827	803	755	—	d	tr	537	480	420	353tr
RM35D	3623d	—	1024	935=	920	826	sh	755	—	d	tr	537	481	421	353tr
LF7	3628	1066	1033	930	?	827	804	754	tr	d	tr	537	480	420	354
LF8	3632	1074d	?	930	?	828	807sh	756	725	687	567	537	478	418	357
RM33	3628	—	1037	939>	917	827	800	756	725tr	d	tr	538	480	421	353tr
LF9	3630	1070d	?	940>	918	829	803	753	727	700d	563	537	478	420	357
RM11	3627d	1066	1028	935>	915	828	805	755	727	690d	566	538	479	417	353
SG4	3632	1072d	1030	935>	917	832	807	755	728	692	565	537	479	418	356
RM12	3632	1065	1026	933>	917	828	805	757	726	688	565	538	479	418	355
SG1	3634	1063	1027	934>	915	833	806	756	727	688	560	538	480	417	355

Note: d = diffuse; — = band not found; Q = quartz; tr = trace; sh = shoulder; <, =, > denote relative intensities at 935 and 915; ? = lack of data.
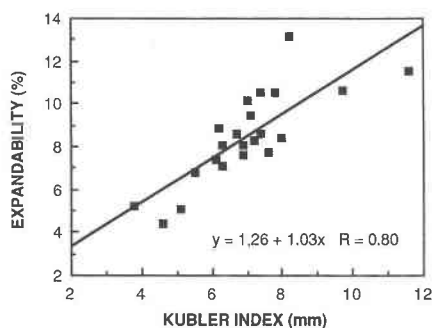
Fig. 13. Relation between the Kubler index ($1° 2\theta = 10$ mm) and expandability (Scherrer method, 26° peak).

by a the lack of a 111 reflection at 3.87 Å and by the splitting of the (201, $\bar{1}$32) peak into two reflections at 2.390 Å and 2.358 Å.

In the other samples that are >6% expandable, $1M$ reflections are weaker, broader, and less complete (Fig. 15, samples RM4, RM22, RM33, RM35A) than are those in the less-expandable clays. Such samples sometimes are termed $1Md$. The 22°–33° band is very pronounced, indicating a large density of rotational faults. Some traces of $2M_1$, with reflections at 3.87, 3.73, 2.99, 2.86, 2.79, 1.729, and 1.521 Å, can be detected in all of these samples; although, in one sample (sample RM35A in Fig. 15), the presence of $2M_1$ cannot be proven unambiguously, because only the 3.87-Å reflection is detectable. This reflection also can result from *cis* or random vacancies in the octahedral sheet of $1M$ structures (Drits et al., 1984). The possibility that this reflection indicates the presence of $3T$ domains was excluded, because the more apparent attributes of this structure, such as a shifting of the 3.06-Å reflection toward smaller angles and a shifting of the 2.92-Å reflection toward larger angles of 2θ (Horton, 1983),

were not observed. The crystallites in this group of samples probably consist of numerous, thin domains of the $1M$ structure, and less abundant $2M_1$ domains, separated by rotational faults. No correlation appears between tridimensional organization and expandability within this group of samples.

SERICITE COMPOSITION

Relation between chemistry and structure

Chemical analyses (Table 7) were converted into structural formulae (Table 8). The relation between fixed-cation content [K + Na, in equivalents per $O_{10}(OH)_2$] and expandability measured by the Scherrer method (26° peak) is shown in Figure 16 ($R = 0.79$). Correlations are $R = 0.74$, 0.63, 0.72, and 0.98 for similar plots in which expandabilities were measured by the Scherrer (17° peak), by deconvolution, by the conventional method, and by the TEM method, respectively. A correlation ($R = 0.86$) also is found between the Kubler index and fixed Na + K, as is shown in Figure 17.

Extrapolation of the line in Figure 16 to pure illite (no expandability) gives a fixed-cation content close to one (1.05 equivalents per half-unit cell), thereby suggesting that the illite layers have a mica charge, with the excess (0.05) in the extrapolated value caused by scatter in the data. Expandabilities measured by the other methods give extrapolated values of 1.00 (Scherrer, 17° peak), 1.09 (deconvolution method), 0.94 (conventional method), and 0.85 (TEM method). These values all suggest that illite layers in the sericites have a fixed-cation content that is larger than that found for illite layers formed by diagenesis in shales and bentonites. Illite layers in diagenetic I/S have an extrapolated fixed-cation content of about 0.75 for end-member illite (Hower and Mowatt, 1966; Šrodoń et al., 1986). Thus the structural and chemical

TABLE 7. Chemical analyses of sericites

| Sample	SiO₂	Al₂O₃	Fe₂O₃	MgO	CaO	Na₂O	K₂O	SrO	TiO₂	F	LOI
AR1	49.6	31.2	1.26	1.90	<0.03	0.07	10.10	0.26	0.09	0.28	5.43
AR1R	51.9	28.2	1.85	1.91	0.03	0.18	9.89	0.55	0.26	0.26	4.57
LF7	48.7	32.7	2.13	0.82	<0.02	0.15	9.05	0.86	0.18	0.18	5.88
LF10	48.5	31.9	2.09	0.95	<0.03	0.25	8.56	1.07	0.07	0.41	6.31
RM3	49.2	31.0	1.96	1.05	0.03	0.13	9.15	0.66	0.70	0.14	7.04
RM4	50.0	30.7	1.78	1.52	<0.03	0.10	9.03	0.81	0.39	0.16	6.97
RM5	49.8	31.2	1.26	1.40	<0.02	0.12	9.25	1.05	0.82	0.14	6.54
RM6	49.7	32.0	0.90	1.34	0.03	0.12	8.93	0.94	0.21	0.15	6.27
RM8	49.1	31.5	2.14	0.85	<0.02	0.15	8.56	1.08	0.42	0.14	6.19
RM11	48.2	33.2	1.09	0.63	0.05	0.11	8.83	1.23	0.42	0.10	6.34
RM12	48.6	33.3	1.24	0.71	0.08	0.16	8.64	1.12	0.07	0.12	6.38
RM13	49.7	30.9	1.48	1.60	<0.03	0.11	9.10	0.95	0.46	0.18	5.58
RM21	49.3	30.9	1.66	1.34	0.07	0.38	7.56	2.30	0.32	0.20	7.65
RM22	48.9	33.3	0.89	0.80	0.03	N.A.	7.55	N.A.	0.58	0.12	6.72
RM28	50.2	31.1	0.05	2.08	<0.04	0.10	9.26	0.78	0.38	0.19	6.07
RM30	48.9	33.0	<0.08	1.38	<0.03	0.10	9.32	0.81	0.33	0.16	5.97
RM31	49.1	31.8	1.37	1.52	0.04	0.19	9.43	0.59	0.16	0.12	5.53
RM35A	49.4	31.4	0.87	1.29	<0.04	0.14	8.27	1.29	0.60	0.23	6.94
RM35C	49.2	32.0	0.99	1.29	<0.02	0.16	8.58	1.04	0.41	0.24	6.38
RM35D	49.9	31.2	1.31	1.30	<0.02	0.16	7.56	2.74	0.21	0.25	7.23
SG1	48.3	33.4	1.20	0.58	0.03	0.20	9.18	0.54	0.17	0.16	5.47
SG4	48.3	33.3	0.42	0.98	<0.03	0.38	9.27	0.33	0.35	0.18	5.25

Note: N.A. = not analyzed; LOI = loss on ignition.
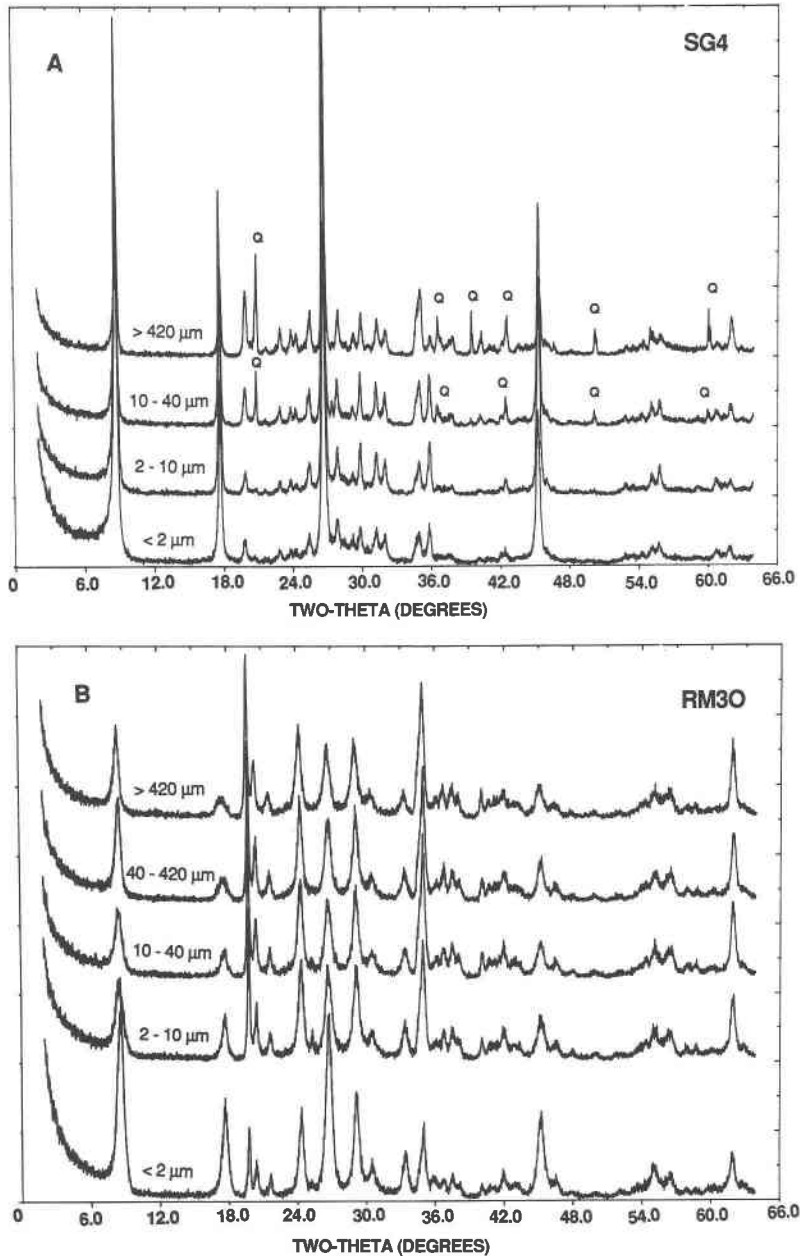
Fig. 14. XRD patterns for randomly oriented sericite preparations having different grain-size fractions. (A) sample SG4; (B) sample RM30; Q = quartz.

evidence indicates that the sericites may be, from the viewpoint of layer charge, very fine grained muscovite or phengite. (Phengite is a mica in which part of the layer charge is developed by Mg for Al substitution in the octahedral sheet.) Their apparently low fixed-cation content in their structural formulae (0.66 to 0.88 equivalents in Table 8) is related to the presence of a large proportion of particle edges and, possibly, to a deficiency (<1.0) of fixed cations in the micaceous interlayers.

The relation between cation-exchange capacity (CEC) and expandability (Scherrer method, 26° peak) for sericite

is evident in Tables 8 and 3 and in Figure 18 ($R = 0.87$). Plots of CEC (in meq Sr^{2+} per 100-g oxide) vs. expandabilities measured by the Scherrer method (17° peak), by deconvolution, and by the conventional method give $R = 0.83$, 0.73, and 0.73, respectively. The TEM method gives the equation $y = -3.3 + 1.5x$, with $R = 0.98$. A good correlation ($R = 0.95$) was found between CEC and the Kubler index (Fig. 19).

No correlation was found between expandability and the chemistry of the silicate layer (^{IV}Al and/or ^{VI}Fe and ^{VI}Mg), a correlation that has been reported for diagenetic
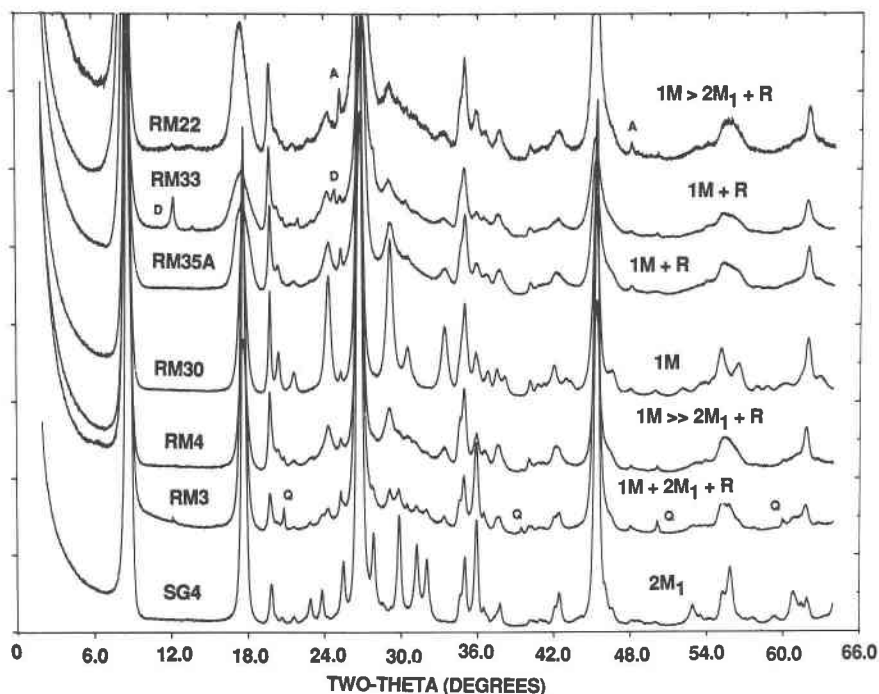
Fig. 15. Sample XRD patterns for randomly oriented sericites ($< 2\ \mu$m) that have a variety of polytypes. A = anatase; D = dickite; Q = quartz. These phases are labeled in the sample patterns in which their lines are the strongest.

I/S formed both in shales (Hower et al., 1976) and in bentonites (Środoń et al., 1986). Also, the sericites are less phengitic than are diagenetic clays of similar expandability (0.1 to 0.3 equivalents Fe + Mg in the sericites, vs. 0.3 to 0.5 in bentonites; Środoń et al., 1986).

Relation between chemistry and infrared (IR) spectra

IR spectra of 20 pure samples (<2-μm fraction in the Sr form) are given in Table 6. Samples are arranged in this table according to the evolving nature of the absorption bands in the 910 to 940 cm^{-1} region. Two representative spectra are shown in Figure 11. All the spectra are characteristic of dioctahedral, aluminous clay minerals that are similar in composition to muscovite (Velde, 1978); however, several subtle variations can be noted, the most pronounced of which is absorption between 910 and 940 cm^{-1}. In some samples, absorption in this region is a single, sharp band at about 916 cm^{-1} (Fig. 11); in

TABLE 8. Structural formulae* and cation-exchange capacities (CEC)** for sericites

Sample	^{IV}Si	^{IV}Al	^{VI}Al	^{VI}Fe	^{VI}Mg	Na	K	Sr	Charge	CEC
AR1	3.30	0.70	1.75	0.06	0.19	0.01	0.86	0.01	0.89	2.5
AR1R	3.45	0.55	1.66	0.09	0.19	0.02	0.84	0.02	0.91	5.3
LF7	3.24	0.76	1.81	0.11	0.08	0.02	0.77	0.03	0.85	8.3
LF10	3.26	0.74	1.79	0.11	0.10	0.03	0.73	0.04	0.85	10.3
RM3	3.31	0.69	1.77	0.01	0.11	0.02	0.79	0.03	0.85	6.3
RM4	3.34	0.66	1.75	0.09	0.15	0.01	0.77	0.03	0.84	7.8
RM5	3.32	0.68	1.78	0.06	0.14	0.02	0.79	0.04	0.88	10.1
RM6	3.31	0.69	1.81	0.05	0.13	0.02	0.76	0.04	0.85	9.0
RM8	3.30	0.70	1.79	0.11	0.09	0.02	0.73	0.04	0.84	10.4
RM11	3.24	0.76	1.87	0.06	0.06	0.01	0.76	0.05	0.87	11.8
RM12	3.24	0.76	1.86	0.06	0.07	0.04	0.73	0.04	0.85	10.8
RM13	3.32	0.68	1.76	0.07	0.16	0.01	0.78	0.04	0.86	9.1
RM21	3.32	0.68	1.77	0.08	0.13	0.07	0.65	0.09	0.89	22.1
RM28	3.35	0.65	1.79	0.0	0.21	0.01	0.79	0.03	0.86	7.5
RM30	3.27	0.73	1.86	0.0	0.14	0.01	0.79	0.03	0.87	7.8
RM31	3.28	0.72	1.78	0.07	0.15	0.02	0.80	0.02	0.88	5.6
RM35A	3.33	0.67	1.82	0.04	0.13	0.02	0.71	0.05	0.83	12.4
RM35C	3.30	0.70	1.82	0.05	0.13	0.02	0.73	0.04	0.83	10.0
RM35D	3.33	0.67	1.78	0.07	0.13	0.02	0.64	0.11	0.88	26.3
SG1	3.24	0.76	1.87	0.06	0.06	0.03	0.78	0.02	0.86	5.1
SG4	3.24	0.76	1.88	0.02	0.10	0.05	0.79	0.01	0.87	3.2

* Equivalents per half-unit cell.
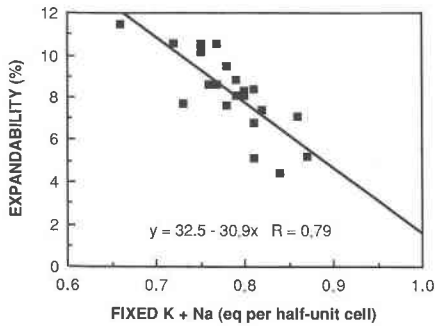** Cation-exchange capacity in meq Sr^{2+} per 100 g of fired clay.

Fig. 16. Relation between fixed-cation content and expandability (Scherrer method, 26° peak).

Fig. 18. Relation between cation-exchange capacity (CEC, in meq per 100 g fired sample) and expandability (Scherrer method, 26° peak).

other samples, this band becomes diffuse towards larger wave numbers, and a second band appears at about 933 cm^{-1}. This change in the 910 to 940 cm^{-1} region is accompanied by (1) a slight shift in the OH stretching vibration, from 3627 to 3634 cm^{-1}; (2) the appearance of a band at 725 cm^{-1} and a shoulder at 885 cm^{-1}, which appear simultaneously with the 935 cm^{-1} band and gradually increase in intensity; (3) an increase in the depth of the valley between the 915- and 830-cm^{-1} bands; (4) an increase in intensity for the 805-cm^{-1} band; (5) a change in the intensity ratio for the bands at 830 and 755 cm^{-1} from 850 > 755, to 850 < 755; and (6) shifts in the Si–O bending vibrations, from 530 to 538, from 475 to 480, and from 420 to 417 cm^{-1}.

All of the changes reported here can also be seen in spectra for synthetic micas lying on the muscovite–Mg-celadonite join (Velde, 1978); thus, these changes may be related either to Al-for-Si substitution in the tetrahedral sheet, or to Mg-for-Al substitution in the octahedral sheet, or to a combination of the two. Our data (Tables 6 and 8) indicate an approximate correlation between the described features and the sum of Fe + Mg in the octahedral sheet, and no correlation with tetrahedral Al. The most sensitive measurement is the shift of the Si–O bending vibration between 540–530 cm^{-1}. The relation between this wave number and octahedral Mg + Fe in equivalents per $O_{10}(OH)_2$ is given in Figure 20. The effect of Mg and Fe content on this absorption band is identical. This conclusion is supported by Stubican and Roy (1961),
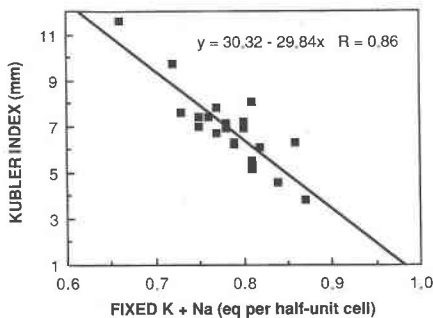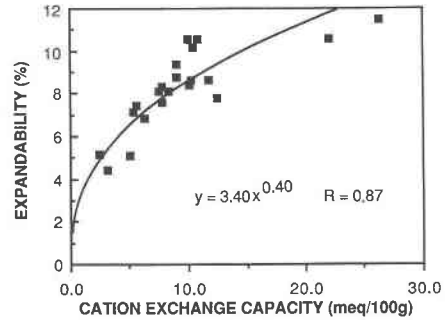
who found nearly the same relation for a synthetic, Fe-free system, and by Hunziker et al. (1986), who found this relation for metamorphic illites from the Glarus Alps, Switzerland. The strong correlation reported by Hunziker et al. (1986) between Mg + Fe and the position of the 060 XRD reflection, however, was not found for sericites from the Silverton caldera.

SERICITE TEXTURES

Size separation performed without grinding yielded as much as 30% by weight of the <2-μm size fraction. No correlation was determined between this yield and expandability. Illite crystallites in the bulk rock and in the various size fractions were determined by SEM to be composed of aggregates of various sizes; however, individual illite crystallites in the aggregates for a given sample were all about the same size.

Crystallite size decreased with increasing expandability, as is illustrated in Figure 21 by samples SG4 (expandability of about 5%) and RM35A (expandability of about 10%). Sample SG4 is composed of well-defined, flat crystallites that are 1–5 μm in diameter and are up to 1000 Å thick. These crystallites most commonly occur in parallel aggregates, but no preferred orientation of these aggregates in the rock was observed. Well-developed *hkl* faces are rare. Sample RM35A is composed of crystallites <2 μm in diameter and <500 Å thick. Typically, the

Fig. 17. Relation between fixed-cation content and the Kubler index.
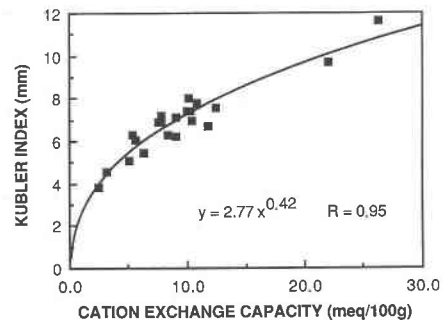

Fig. 19. Relation between cation-exchange capacity (CEC, in meq per 100 g fired sample) and Kubler index.
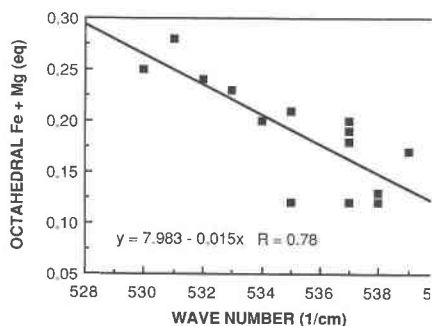
Fig. 20. Relation between the wave number of the infrared-absorption band that migrates between 530 and 539 cm^{-1} and the sum of octahedral Fe + Mg [per $O_{10}(OH)_2$].

crystallites are curved and stick to each other to form curved surfaces on which individual particles are difficult to distinguish. Samples with expandabilities between those of samples SG4 and RM35A have intermediate textures under the SEM. Thus, qualitatively, the thickness of illite particles seen with the SEM agrees with TEM data and fits the hypothesis that expandability is related to illite-particle thickness.

The morphology of individual illite particles seen under the TEM is shown in Figure 6. Pt shadows, used to measure particle thicknesses parallel to c^*, appear as bright areas on the left sides of the particles. Figure 6 offers insight into the reason why illitic material swells, whereas, for example, clay-size quartz does not. Illitic material has expandable layers because these particles have large, flat, electrically charged basal surfaces that can adsorb water and/or organic molecules and can interact with adjacent, superimposed surfaces. Expandability can be detected by XRD, because the particles are so thin that these surfaces compose a significant proportion of the sample.

SERICITE ORIGIN

It would be useful geologically to determine the conditions that caused the subtly diverse mineralogies determined for sericite. K-Ar ages and oxygen-isotope measurements were used to help solve this problem.

Time of formation

Previous work has shown that illitic material is a very good K-Ar clock (Aronson and Lee, 1986) and that the K-Ar technique can be used to date diagenetic events in a variety of geologic settings (Lee et al., 1985; Glassmann, 1985; Lee, 1984; Aronson and Burtner, 1983; Law, 1983). The ages of eight sericites from the Silverton caldera were determined by the K-Ar method; results are presented in Table 9. Two ages are represented: about 21 Ma for the RM samples and about 13 Ma for samples SG4 and AR1. In addition, one sample (sample RM28) had an intermediate age.

Previous work supports the K-Ar ages of the present study. At least two ages for hydrothermal alteration were
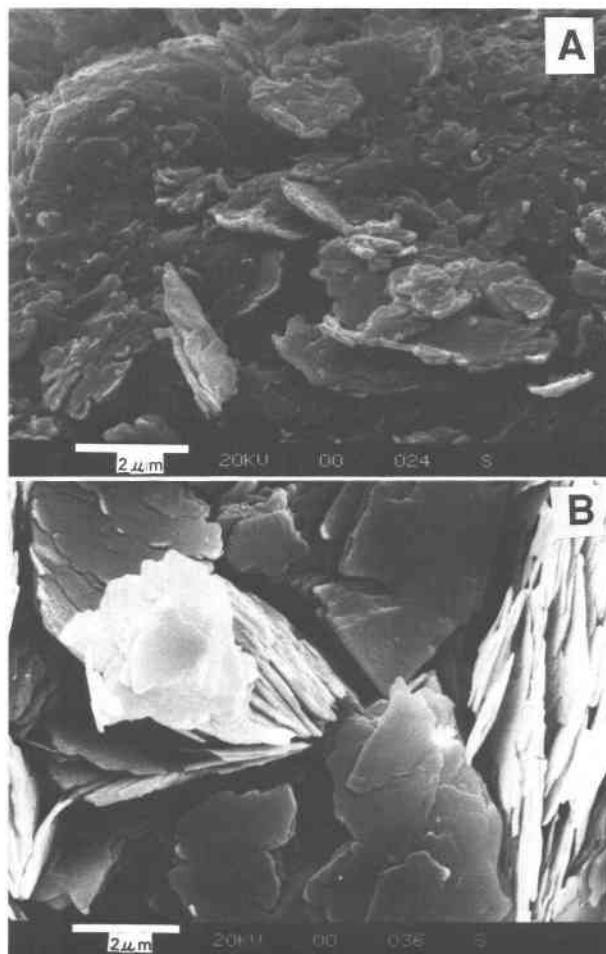

Fig. 21. SEM photographs of two sericites that represent a range of expandabilities. Sample RM35A (expandability of about 10%) is at the top, and sample SG4 (expandability of about 5%) is at the bottom.

determined by Lipman et al. (1976) by dating a variety of minerals in the Silverton caldera–Eureka graben area, both by K-Ar (sanidine and biotite phenocrysts) and by fission-track (zircon and apatite) methods. Their K-Ar ages centered around 11.3 and 22.6 Ma, with one intermediate age at 17 Ma; fission-track ages centered around 12.1 and 21.4 Ma. Casadevall and Ohmoto (1977) dated specimens from the Sunnyside mine (located in the Sil-

TABLE 9. K-Ar age data for sericites

Sample	K$_2$O (%)	Age (m.y.)	Error (m.y.)	Ar* (%)
AR1	10.19	12.1	0.6	72.8
RM5	8.58	21.1	1	72.2
RM8	8.65	21.5	1	71.9
RM28	9.33	17.4	0.8	66.3
RM30	9.42	20	0.9	70.6
RM35A	8.32	20.3	1	59.8
RM35D	7.59	20.2	1	63.7
SG4	9.56	13.8	0.7	56.1

TABLE 10. Oxygen-isotope data

Sample	$\delta^{18}O$		
	Sericite	Quartz	Dickite
AR1	−8.4, −8.1	5.2	
AR1R	−6.9		
SG4	−5.3	−1.1	
SG1	−2.4		
RM28	0.3, 0.6	10.9, 11.1	
RM6	0.7		
RM8	1.0		
RM5	1.1		
RM11	1.1		
LF7	1.3		
RM12	1.3		
RM30	1.4	4.4	
LF8	1.4		
RM35A	1.6, 1.4	8.2	
RM35D	1.7		
RM3	2.4		
RM25			−4.5

verton caldera, about 10 km northeast of the town of Silverton, between the locations of samples SG4 and AR1; see Fig. 1) by the Rb-Sr method and determined an age of 13 Ma for rocks that have large Rb/Sr weight ratios (16.6 Ma if rocks with small Rb/Sr ratios also are included).

The time of Silverton caldera formation was 27.5 Ma (Lipman et al., 1973), which was the time when fractures were formed that would later be conduits for hydrothermal fluids. The 21-Ma hydrothermal event is approximately the time of the formation of the Lake City caldera 25 km to the northeast; of the intrusion of quartz latite dikes, plugs, and breccia pipes, with associated mineralization, in the Silverton caldera; and of the resurgence of the Red Mountain dome, the western margin of which is located less than 1.5 km from the sampling sites for RM5 and RM8. The 13-Ma hydrothermal event was a higher-temperature hydrothermal alteration associated with heated meteoric water that moved through the caldera from south to north (Casadevall and Ohmoto, 1977). The 17-Ma age probably results from a partial overprinting of the older event by the younger event, an interpretation that is supported by a set of samples from the Red Mountain resurgent dome (Lipman et al., 1976) in which zircon gave old ages of 23 to 21 Ma and apatite gave consistently younger ages of 12.9 to 12.3 Ma. These data suggest that the Red Mountain area experienced a high-temperature

event that had little influence on the zircon fission-track ages, but that reset the apatite fission-track systematics. This interpretation also is supported by oxygen-isotope data, to be discussed below.

Temperature of formation

Oxygen-isotope data (Table 10) indicate two groups of $\delta^{18}O$ values for sericite: the RM and LF samples have values that range between 0 and +2.5‰ (relative to SMOW), and the SG and AR samples have values that are 2.5 to 8.5‰ lighter. The data in Table 10 also indicate that there may be two quartz populations: one with values near 0‰, and the other with values from 8 to 11‰, with two samples having intermediate values.

As discussed above, the two oxygen-isotope populations of sericite (RM and SG-AR samples) are separated in time of formation by 7 m.y. Assuming that the sericites formed at isotopic equilibrium with the hydrothermal fluids, the difference in oxygen-isotope values for the two sets of samples requires either two isotopically different formation waters or a large temperature difference at the time of sericite formation. Temperatures and oxygen-isotope compositions of water were calculated from cogenetic quartz crystals, using the illite-water fractionation factor from Eslinger and Savin (1973a) and the quartz-water fractionation factor from Clayton et al. (1972).

The difference in calculated oxygen-isotope compositions of water between samples SG4 and RM35A is small, about 1‰ (Table 11), and the water appears to have been oxygen-shifted, meteoric water (see also Casadevall and Ohmoto, 1977). Thus, the difference in isotopic composition between the older and the younger sericites most likely is related to a difference in temperature at the time of formation. The other sericite-quartz pairs listed in Table 11 most likely are at isotopic disequilibrium, because the calculated temperatures for sericite formation are unlikely for I/S having the reported expandabilities (Horton, 1985). These pairs most likely are mixtures of high- and low-temperature quartz or sericite or both.

Other minerals associated with the RM sericites also indicate that clays in the fractures have undergone two periods of hydrothermal alteration. An oxygen-isotope value for a dickite (sample RM25, Table 10), which occurs in veins and pods surrounded by sericite (sample RM26), cannot be in isotopic equilibrium with any of the

TABLE 11. Isotopic temperatures and water-of-formation compositions calculated from quartz-illite pairs

Sample	Δ Quartz-illite	Calculated temperature of formation (°C)	Water $\delta^{18}O$ at temperature	Comments
RM35A	6.6	178	−6.0	21-Ma lower-temperature event
SG4	4.6	322	−7.0	13-Ma higher-temperature event
RM28	10.4	62	−16.0	mixture of 21- and 13-Ma sericite
RM30	3.0	665	3.5	mixture of 21- and 13-Ma quartz
AR1	13.3	16	−32.4	mixture of 21- and 13-Ma quartz

RM sericites, based on the kaolinite-water fractionation factor. Both the dickite and the disequilibrium quartz mentioned before may have been formed by the younger, higher-temperature hydrothermal event that formed the SG and AR sericites. To test this possibility, the temperature of dickite formation was calculated using the kaolinite fractionation factor from Taylor (1976), and a water composition calculated from sample SG4 (Table 11). The calculated temperature for dickite formation by this method is 312°C, which is similar to the temperature of formation of sample SG4 (322°C).

In addition, the sericite that has an intermediate age (sample RM28, Table 9) also has an intermediate $\delta^{18}O$ value (Table 10) lying between that of the high- and low-temperature sericites. Thus, both stable- and radiogenic-isotope data support the conclusion that sample RM28 is a mixture of the two generations of sericite.

Expandability measurements and polytype information support the conclusion drawn from the stable-isotope data that the temperature of the older alteration was lower than that of the younger alteration. The 20-Ma sericite (sample RM35A, 178°C, Table 11) is predominantly $1M$, with some random stacking (Table 1), and has an expandability of about 10%. I/S of this expandability was reported to form in hydrothermally altered rocks at about 175°C in Pliocene and Pleistocene sedimentary rocks from the Imperial Valley, California (Jennings and Thompson, 1986), at about 185°C in borehole Elmore 1 in the Salton Sea geothermal field, California (McDowell and Elders, 1980), and at about 195°C ± 15°C (Fig. 11 in Horton, 1985) based on a compilation from several authors. In diagenetically altered Carboniferous sedimentary rocks from central Poland, however, 10% expandable I/S corresponds to a temperature of about 110 to 120°C (Środoń, 1984). The 13.8-Ma sericite (sample SG4, 322°C, Table 11) is $2M_1$ (Table 1) and has an expandability of about 5%. Its isotopic temperature agrees with a temperature range of 270 to 321°C inferred by Casadevall and Ohmoto (1977) for the formation of this generation of sericite at the Sunnyside mine from measurements of the filling temperatures of fluid inclusions in quartz. Weaver and Associates (1984), extrapolating the isotopic data of Eslinger and Savin (1973a, 1973b), estimated that only the $2M_1$ polytype would exist in shale that had been heated to 400°C. Mica-synthesis experiments have indicated that the following polytypes form with increasing temperature (Velde, 1965; Yoder and Eugster, 1955): $1Md \rightarrow 1M \rightarrow 2M_1$. This sequence also supports the present data.

According to a classification based on Kubler indices, all of the sericites except AR1 (Table 3) fall into the "diagenesis" grade of metamorphism (Kubler index > 4.2, assuming $1° 2\theta = 10$ mm on the X-ray chart). In studies of Alpine metamorphism, the diagenesis grade corresponds to temperatures <200°C (Frey, 1986). Based on the isotopic temperatures discussed above, however, it is evident that the relation between temperature and Kubler index for our hydrothermal sericites, especially for the younger, higher-temperature suite, is not the same as that found for the Alpine metamorphic illites. This lack of correlation is not unexpected, however, because illites in shales may be a mixture of two phases: higher-temperature detrital and lower-temperature diagenetic illite (Środoń and Eberl, 1984).

DISCUSSION

Sericite from the Silverton caldera is composed of particles that contain muscovite or phengite layers. Its composition and structure deviate significantly from those of coarser-grained micas, however, because its particle size is so small. The thinner the particles, the larger the proportion of exposed basal surfaces, the greater the CEC, the smaller the amount of fixed interlayer cations in the structural formulae, and the larger the expandability.

Terminology for this material is confused, because its name depends on how it is studied. The optical microscope reveals sericite, whereas the TEM shows individual mica particles and XRD gives patterns for mixed-layer illite/smectite. Chemical analyses and expandability measurements (Scherrer method, Fig. 16) approximately give a full complement of fixed interlayer cations (1.0 equivalents per half-unit cell) for individual mica layers, and a lower fixed-cation content when particle edges are included in the structural formulae. Part of the terminology problem originates from the definition of the word "mineral," which requires that crystal structure and chemical composition be specified. This definition works well for larger crystals, but for sericite a third parameter—particle thickness—influences the mineral's properties. Particle edges, which compose a significant proportion of the mineral, do not have well-defined structure and composition.

These hydrothermal illite/smectites differ from I/S formed by diagenesis in shales and bentonites. The hydrothermal clays show no correlation between 2:1 layer chemistry and expandability, whereas ^{IV}Al increases as expandability decreases in diagenetic clays. The hydrothermal I/S have a larger, extrapolated, average content of fixed interlayer cations per illite layer (0.85 to 1.0, depending on which expandability method is used) than do the diagenetic clays (0.75). Also, mixtures of hydrothermal polytypes cannot be separated by grain size, whereas $2M_1$ polytypes in shales frequently occur in a coarser size fraction than do $1M$ and $1M_d$ polytypes. These differences between hydrothermal and diagenetic I/S may be a function of mode of formation: precipitation from solution for the hydrothermal clays vs. alteration of precursor smectite for the shales and bentonites.

Expandability measurements have proven to be useful in understanding the geologic history of rocks and sediments. Expandability of I/S has been correlated with temperature (Perry and Hower, 1970; Hoffman and Hower, 1979); with reaction time (Eberl and Hower, 1976); with the charge density and chemistry of the original smectite (Środoń, 1976; Eberl et al., 1978); with the availability of K and with pH (Altaner et al., 1984; Środoń and Eberl, 1984; Eberl et al., 1986); with proximity to the thermal

effects of plutons, veins, and dikes (Nadeau and Reynolds, 1981; Horton, 1983, 1985; Lynch, 1985); with the volume of subsurface water flow (Whitney and Northrop, 1987); with the degree of leaching of pre-existing illite (Rimmer and Eberl, 1982; results of Chamley et al. summarized by Singer, 1984); and with the number of wetting and drying cycles experienced by smectite in the presence of K (Eberl et al., 1986). Thus, accurate expandability measurements may be important for understanding the geologic history of deposits that contain sericite.

Three XRD methods for measuring the expandabilities of sericite were presented: the conventional method, the deconvolution method, and the Scherrer method. The Scherrer method, which is the easiest method to apply, yields expandabilities that correlate best with other parameters such as particle thickness, fixed-interlayer-cation content, CEC, the Kubler index (thereby suggesting that this "crystallinity" index is a function of illite-particle thickness), the intensity ratio (Ir), and the wave number of the 824–834 cm^{-1} infrared absorption band, especially when the breadth of the 26° peak is used. Therefore the Scherrer method (26° peak) may be the most precise XRD method. The TEM method also gave very good (although somewhat different) correlations. More TEM measurements are needed to determine which method is the more accurate.

Because expandability for sericite is a measure of mean particle thickness (Eq. 1), the expandability of sericite in hydrothermal deposits could be a function of numerous factors that can affect the growth of illite crystals parallel to c^*. These factors could include the mechanism and the rate of crystallization; the presence or absence of crystal-growth inhibitors and modifiers; the availability of nutrient solutions; the availability of pore space; and the chemistry, structure, and solubility of precursor materials, etc. The important petrologic question, therefore, is not whether I/S of various expandabilities are thermodynamically stable, but, rather, what conditions give rise to the various particle-size distributions for illite?

Fluid-inclusion data for similar clays in the eastern San Juan Mountains (Creede caldera) indicate that the most important factor that influences expandability is temperature (Horton, 1985). This determination generally agrees with our data, which indicate that the younger, higher-temperature sericites are the least expandable; however, an exact correlation between expandability and temperature cannot be made from the present data set.

Finally, one can speculate concerning the thermodynamic stability of sericites having a range of expandabilities. If expandability is simply a measure of mean particle thickness, then, according to the traditional definition of "mineral" that does not consider particle size, all of the mixed-layer I/S examined here is illite (or muscovite or phengite, depending on how these terms are defined), as has been suggested previously by Nadeau et al. (1984a, 1984b). An "ordered I/S" is an illite with a narrow particle-size distribution; there is no smectite *phase* present, unless, for some applications, the edges of particles can

be considered to be a separate phase. (Values for the free energy of formation for sericite should be affected considerably by the proportion of these edges; see, for example, Page and Wenk, 1979.) From this viewpoint, I/S of low expandability is neither a solid solution nor a mixture of phases (Garrels, 1984), but it is a single, thermodynamically stable phase that forms under a specific range of thermochemical conditions. Information concerning this range of conditions, however, can be gained by accurately determining illite particle thickness (expandability).

REFERENCES

Altaner, S.P., Hower, J., Whitney, G., and Aronson, J. L. (1984) Model for K-bentonite formation: Evidence from zoned K-bentonites in the disturbed belt, Montana. Geology, 12, 412–425.

Aronson, J.L., and Burtner, R.L. (1983) K/Ar dating of illitic clays in Jurassic Nugget Sandstone and timing of petroleum migration in Wyoming Overthrust Belt: American Association of Petroleum Geologists Bulletin, 67, 414.

Aronson, J.L., and Lee, M. (1986) K/Ar systematics of bentonite and shale in a contact metamorphic zone, Cerrillos, New Mexico. Clays and Clay Minerals, 34, 483–487.

Beaufort, D., and Meunier, A. (1983) A petrographic study of phyllic alteration superimposed on potassic alteration: The Silbert porphyry deposit (Rhone, France). Economic Geology, 78, 1514–1527.

Bethke, C.M., and Reynolds, R.C. (1986) Recursive method for determining frequency factors in interstratified clay diffraction calculations. Clays and Clay Minerals, 34, 224–226.

Bonorino, F.G. (1959) Hydrothermal alteration in the Front Range mineral belt, Colorado. Geological Society of America Bulletin, 70, 53–90.

Brindley, G.W. (1980) Order-disorder in clay mineral structures. In G.W. Brindley and G. Brown, Eds., Crystal structures of clay minerals and their X-ray identification, p. 249–303. Mineralogical Society, London.

Burbank, W.S., and Luedke, R.G. (1961) Origin and evolution of ore and gangue-forming solutions, Silverton caldera, Colorado. U.S. Geological Survey Professional Paper, 424-C, C7–C11.

Casadevall, T., and Ohmoto, H. (1977) Sunnyside mine, Eureka mining district, San Juan County, Colorado: Geochemistry of gold and base metal ore deposition in a volcanic environment. Economic Geology, 72, 1285–1320.

Cathelineau, M. (1983) Les minéraux phylliteux dans les gisements hydrothermaux d'uranium. II. Distribution et évolution cristallochimique des illites interstratifiés, smectites et chlorites. Bulletin de Minéralogie, 106, 553–569.

Clayton, R.N., and Mayeda, T.K. (1963) The use of bromine pentafluoride in the extraction of oxygen from oxides and silicates for isotopic analysis. Geochimica et Cosmochimica Acta, 27, 43–52.

Clayton, R.N., O'Neil, J.R., and Mayeda, T.K. (1972) Oxygen isotope exchange between quartz and water. Journal of Geophysical Research, 77, 3057–3067.

Drits, V.A., Plançon, A., Sakharov, B.A., Besson, G., Tsipursky, S.I., and Tchoubar, C. (1984) Diffraction effects calculated for structural models

of K-saturated montmorillonite containing different types of defects. Clay Minerals, 19, 541–561.

Eberl, D.D., and Hower, J. (1976) Kinetics of illite formation. Geological Society of America Bulletin, 87, 1326–1330.

Eberl, D., Whitney, G., and Khoury, H. (1978) Hydrothermal reactivity of smectite. American Mineralogist, 63, 401–409.

Eberl, D.D., Šrodoń, J., and Northrop, H.R. (1986) Potassium fixation in smectite by wetting and drying. In J.A. Davis and K.F. Hayes, Eds., Geochemical processes at mineral surfaces. American Chemical Society Symposium Series, 323, 296–326.

Eslinger, E.V., and Savin, S.M. (1973a) Mineralogy and oxygen-isotope geothermometry of the hydrothermally altered rocks of the Ohaki-Broadlands, New Zealand, geothermal area. American Journal of Science, 273, 240–267.

——— (1973b) Oxygen-isotope geothermometry of the burial metamorphism rocks of the Precambrian Belt Supergroup, Glacier National Park, Montana. Geological Society of America Bulletin, 84, 2549–2560.

Frey, M. (1986) Very low-grade metamorphism of the Alps—An introduction. Schweizerische Mineralogische und Petrographische Mitteilungen, 66, 13–27.

Garrels, R.M. (1984) Montmorillonite/illite stability diagrams. Clays and Clay Minerals, 32, 161–166.

Glasmann, J.R. (1985) Smectite diagenesis in bentonites of the Shale Wall Member of the Seabee Formation, North Slope, Alaska (abs.). American Association of Petroleum Geologists Research Conference, Radiogenic isotopes and evolution of sedimentary basins, New Orleans, Louisiana.

Hendry, D.A.F. (1981) Chlorites, phengites, and siderites from the Prince Lyell ore deposit, Tasmania, and the origin of the deposit. Economic Geology, 76, 285–303.

Hoffman, J., and Hower, J. (1979) Clay mineral assemblages as low grade metamorphic geothermometers: Application to thrust faulted disturbed belt of Montana, U.S.A. In P.A. Scholle and P.R. Schluger, Eds., Aspects of diagenesis. Society of Economic Paleontologists and Mineralogists Special Publication, 26, 55–79.

Horton, D.G. (1983) Argillic alteration associated with the Amethyst vein system, Creede mining district, Colorado. Ph.D. thesis, University of Illinois, Urbana, Illinois.

——— (1985) Mixed-layer illite/smectite as a paleotemperature indicator in the Amethyst vein system, Creede district, Colorado, USA. Contributions to Mineralogy and Petrology, 91, 171–179.

Hower, J., and Mowatt, T.C. (1966) The mineralogy of illites and mixed-layer illite-montmorillonites. American Mineralogist, 51, 825–854.

Hower, J., Eslinger, E.V., Hower, M.E., and Perry, E.A. (1976) Mechanism of burial metamorphism of argillaceous sediments: 1. Mineralogical and chemical evidence. Geological Society of America Bulletin, 87, 725–737.

Hunziker, J.C., Frey, M., Clauer, N., Dallmeyer, R.D., Friedrichsen, H., Flehmig, W., Hochstrasser, K., Roggwiler, P., and Schwander, H. (1986) The evolution of illite to muscovite: Mineralogical and isotopic data from the Glarus Alps, Switzerland. Contributions to Mineralogy and Petrology, 92, 157–180.

Jackson, M.L. (1975) Soil chemical analysis—advanced course. Published by the author, Madison, Wisconsin.

Jennings, S., and Thompson, G.R. (1986) Diagenesis of Plio-Pleistocene sediments of the Colorado River delta, southern California. Journal of Sedimentary Petrology, 56, 89–98.

Kisch, H.J. (1983) Mineralogy and petrology of burial diagenesis (burial metamorphism) and incipient metamorphism in clastic rocks. In G. Larsen and G.V. Chilingar, Eds., Diagenesis in sediments and sedimentary rocks, Developments in Sedimentology 25B, p. 289–494. Elsevier, New York.

Klug, H.P., and Alexander, L.E. (1974) X-ray diffraction procedures. Wiley, New York.

Law, E. (1983) Petrologic, geochronologic, and isotopic investigations of the diagenesis and hydrocarbon emplacement in the Muddy Sandstone, Powder River Basin. Ph.D. thesis, Case Western Reserve University, Cleveland, Ohio.

Le Bel, L. (1979) Micas magmatiques et hydrothermaux dans l'environnement du porphyre cuprifère de Cerro Verde–Santa Rosa, Perou. Bulletin de Minéralogie, 102, 35–41.

Lee, M. (1984) Diagenesis of the Permian Rotligenedes Sandstone, North Sea: K/Ar, O18/O16, and petrologic evidence. Ph.D. thesis, Case Western Reserve University, Cleveland, Ohio.

Lee, M., Aronson, J.L., and Savin, S.M. (1985) K/Ar dating of time of gas emplacement in Rotliegendes Sandstone, Netherlands. American Association of Petroleum Geologists Bulletin, 69, 1381–1385.

Leedy, W.P. (1971) Hydrothermal alteration of volcanic rocks in the Red Mountains District of the San Juan Mountains, Colorado. Ph.D. thesis, State University of New York at Buffalo, Buffalo, New York.

Lipman, P.W., Steven, T.A., and Mehnert, H.H. (1970) Volcanic history of the San Juan Mountains, Colorado, as indicated by potassium-argon dating. Geological Society of America Bulletin, 81, 2329–2352.

Lipman, P.W., Steven, T.A., Leudke, R.G., and Burbank, W.S. (1973) Revised history of the San Juan, Uncompahgre, Silverton, and Lake City calderas in the western San Juan Mountains, Colorado. U.S. Geological Survey Journal of Research, 1, 627–642.

Lipman, P.W., Fisher, F.S., Mehnert, H.H., Naeser, C.W., Luedke, R.G., and Steven, T.A. (1976) Multiple ages of mid-Tertiary mineralization and alteration in the western San Juan Mountains, Colorado. Economic Geology, 71, 571–588.

Lowell, J.D., and Guilbert, J.M. (1970) Lateral and vertical alteration-mineralization zoning in porphyry ore deposits. Economic Geology, 65, 373–408.

Luedke, R.G., and Hosterman, J.W. (1971) Clay minerals, Longfellow mine, San Juan County, Colorado. U.S. Geological Survey Professional Paper 750-C, C104–C111.

Lynch, L.F., III (1985) The stoichiometry of the smectite to illite reaction in a contact metamorphic environment. Master's thesis, Dartmouth College, Hanover, New Hampshire.

Marquardt, D.M. (1963) An algorithm for least-squares estimation of nonlinear parameters. Journal of the Society for Industrial and Applied Mathematics, 11, 431–441.

McDowell, S.D., and Elders, W.A. (1980) Authigenic layer silicate minerals in borehole Elmore 1, Salton Sea geothermal field, California, USA. Contributions to Mineralogy and Petrology, 74, 293–310.

Meunier, A., and Velde, B. (1982) Phengitization, sericitization and potassium-beidellite in a hydrothermally-altered granite. Clay Minerals, 17, 285–299.

Muller-Koelbl, G. (1986) Examples for the fit program. Siemens Application Note No. 75, Siemens Energy & Automation, Inc., 1 Computer Drive, Cherry Hill, N. J. 08034.

Nadeau, P.H. (1985) The physical dimensions of fundamental clay particles. Clay Minerals, 20, 499–514.

Nadeau, P.H., and Reynolds, R.C., Jr. (1981) Burial metamorphism in the Mancos Shale. Clays and Clay Minerals, 29, 249–259.

Nadeau, P.H., Wilson, M.J., McHardy, W.J., and Tait, J.M. (1984a) Interparticle diffraction: A new concept for interstratified clays. Clay Minerals, 19, 757–769.

——— (1984b) Interstratified clays as fundamental particles. Science, 225, 923–925.

Nicot, E. (1981) Les phyllosilicates des terrains précambriens du Nord-Ouest du Montana (U.S.A.) dans la transition anchizone-épizone. Bulletin de Minéralogie, 104, 615–624.

Omelyanenko, B.T., Volovikova, I.M., Drits, V.A., Zvyagin, B.B. Andreev, O. V., and Sakharov, B.A. (1982) On the content of sericite notion. Izvestiya Akademii Nauk SSSR, Seriya Geologicheskaya no. 5, 69–86.

Page, R., and Wenk, H.-R. (1979) Phyllosilicate alteration of plagioclase studied by transmission electron microscopy. Geology, 7, 393–397.

Parry, W.T., Ballantyne, J.M., and Jacobs, D.C. (1984) Geochemistry of hydrothermal sericite from Roosevelt Hot Springs and the Tintic and Santa Rita porphyry copper systems. Economic Geology, 79, 72–86.

Perry, E.A., and Hower, J. (1970) Burial diagenesis in Gulf Coast pelitic sediments. Clays and Clay Minerals, 18, 165–177.

Reynolds, R.C. (1980) Interstratified clay minerals. In G.W. Brindley and G. Brown, Eds., Crystal structures of clay minerals and their X-ray identification, p. 249–303, Mineralogical Society, London.

Rimmer, S.M., and Eberl, D.D. (1982) Origin of an underclay as revealed by vertical variations in mineralogy and chemistry. Clays and Clay Minerals, 30, 422–430.

Schramm, L.L., and Kwak, J.C.T. (1980) Application of ultrafiltration/

dialysis to the preparation of clay suspensions. Clays and Clay Minerals, 28, 67–69.

Shirozu, H., and Higashi, S. (1972) X-ray examination of sericite minerals associated with the Kuroko deposits. Clay Science, 4, 137–142.

Singer, A. (1984) The paleoclimatic interpretation of clay minerals in sediments—A review. Earth-Science Reviews, 21, 251–293.

Sokolova, T.N., Sakharov, B.A., Drits, V.A., and Kremenetskaya, T.N. (1978) Leucophyllite-montmorillonite mixed-layer minerals from the Inder dome gypsum hat. Lithology and Mineral Resources, 13, 722–733.

Środoń, J. (1976) Mixed-layer smectite/illites in the bentonites and tonsteins of the Upper Silesian Coal Basin. Prace Mineralogiczne, 49, 1–84.

———(1980) Precise identification of illite/smectite interstratifications by X-ray powder diffraction. Clays and Clay Minerals, 28, 401–411.

———(1984) X-ray identification of illitic materials. Clays and Clay Minerals, 32, 337–349.

Środoń, J., and Eberl, D.D. (1984) Illite. Mineralogical Society of America Reviews in Mineralogy, 495–544.

Środoń, J., Morgan, D.J., Eslinger, E.V., Eberl, D.D., and Karlinger, M.R. (1986) Chemistry of illite/smectite and end-member illite. Clays and Clay Minerals, 34, 368–378.

Steiger, R.H., and Jager, E. (1977) Subcommission on geochronology: Convention on the use of decay constant in geo- and cosmochronology. Earth and Planetary Science Letters, 36, 359–362.

Stubican, V., and Roy, R. (1961) Isomorphous substitution and the infrared spectra of layer lattice silicates. American Mineralogist, 46, 32–51.

Taggart, J.E., Lichte, F.E., and Wahlberg, J.S. (1981) Methods of analysis of samples using X-ray fluorescence and induction-coupled plasma spectroscopy. U.S. Geological Survey Professional Paper 1250, 683–687.

Taylor, H.P., Jr. (1976) Oxygen and hydrogen isotope relationships in hydrothermal mineral deposits. In H.L. Barnes, Ed., Geochemistry of hydrothermal ore deposits, p. 236–277. Wiley, New York.

Van Loon, J.C., and Parissis, C.M. (1969) Scheme of silicate analysis based on the lithium metaborate fusion followed by atomic-absorption spectrometry. The Analyst, 94, 1057–1062.

Velde, B. (1965) Phengite micas: Synthesis, stability, and natural occurrence. American Journal of Science, 263, 886–913.

———(1978) Infrared spectra of synthetic micas in the series muscovite–MgAl celadonite. American Mineralogist, 63, 343–349.

Weaver, C.E., and Associates. (1984) Shale-slate metamorphism in southern Appalachians. Developments in Petrology, 10. Elsevier, New York.

Whitney, G., and Northrop, H.R. (1987) Diagenesis and fluid flow in the San Juan Basin, New Mexico—Regional zonation in the mineralogy and stable isotope composition of clay minerals in sandstone. American Journal of Science, 287, 353–382.

Yoder, H.S., and Eugster, H.P. (1955) Synthetic and natural muscovites. Geochimica et Cosmochimica Acta, 8, 225–280.